Operation-Aware Deterministic Global Optimization of Carnot Battery Design using Hybrid Modeling

Jannik T. Lüthje[1], Marco Langiu[1], and Alexander Mitsos[2,1,3]

[1]Process Systems Engineering (AVT.SVT), RWTH Aachen University, Forckenbeckstr. 51, Aachen 52074, Germany
[2]JARA-ENERGY, Templergraben 55, Aachen 52056, Germany
[3]Energy Systems Engineering (ICE-1), Forschungszentrum Jülich, Wilhelm-Johnen-Straße, Jülich 52425, Germany

June 24, 2026

Abstract

The global demand for grid-scale energy storage continues to increase. Carnot batteries (CBs) are not geographically constrained and consist of mature components. Furthermore, charging power, discharging power, and storage capacity can be sized independently and tailored to the intended use case. Designing an optimal CB also requires considering the resulting operational behavior. While design and operation are frequently addressed separately, only simultaneous consideration can ensure an overall optimum. To this end, we extend our hybrid mechanistic/data-driven reduced-space CB model, used for working fluid (WF) screening in Lüthje et al. (2026) [Optim Eng, 27, 587–616], to include component sizing, cost correlations, and optimal operation for price arbitrage in the German day-ahead market. To reduce computational complexity, we solve both heat transfer calculations and the optimal operation problem offline, and embed surrogate models, respectively predicting heat transfer coefficients and revenue as functions of the battery parameters. We compute the Pareto curve between capital cost minimization and revenue maximization for a CB with a nominal charging power of 50 MW using MAiNGO v0.10.2, applying reliability branching to improve performance. Throughout, we consider deterministic global optimization, noting that by definition, the Pareto curve considers global solutions. Results vary strongly with the considered electricity price profile and WF. A CB, without restrictions on the choice of WF, would have been profitable in the German day-ahead market in 2022 and 2024. However, this is not the case when only non-toxic, environmentally friendly WFs are considered, emphasizing the importance of research on novel WFs.

Acknowledgments

The authors gratefully acknowledge the financial support of the Kopernikus project SynErgie by the Federal Ministry of Research, Technology and Space (BMFTR) and the project supervision by the project management organization Projektträger Jülich (PtJ). Computations were performed with computing resources granted by RWTH Aachen University.

1 Introduction

Demand for grid-scale electricity storage is ever-increasing due to the growing share of renewable energy sources (Cebulla et al. 2018). Carnot batterys (CBs) are a potential option to fulfill a part of this demand, as they consist of technologically mature components, are location-independent, and exhibit a long lifetime. For reviews of CBs, we refer to Dumont et al. (2020), Liang et al. (2022), and Lykas et al. (2026). In CBs, electricity is first converted to heat in a power to heat (P2H) process, which is then stored in a thermal energy storage (TES). During periods of high electricity prices or higher electricity demand, the heat is converted back into electricity via a heat to power (H2P) process.

Many options exist to implement P2H, TES, and H2P. For TES, we differentiate between so-called "sensible" TES and "latent" TES (Liang et al. 2022). Sensible storage uses heat to increase the temperature of a storage medium, with pressurized water, molten salt, and thermal oils being common storage media. Latent storage exploits the latent heat of fusion of the storage medium, i.e., thermal energy is stored and released at a (mostly) constant temperature, by melting and solidifying a phase-change material (PCM). For P2H and H2P, the two most used processes are Brayton-based cycles and Rankine-based cycles. Brayton-based CBs use a reverse Brayton cycle for charging and a standard Brayton cycle for discharging. They require high temperature differences in the TES, restricting the storage material selection, and are limited by maximum compressor discharge temperatures (∼500 °C, Dumont et al. 2020). Rankine-based CBs use a vapor-compression heat pump (HP) for charging and a Rankine cycle or Organic Rankine cycle (ORC) for discharging. These CBs operate at lower temperatures and achieve higher energy densities (Steinmann 2014).

Schmidt et al. (2019) define 12 core applications for electricity storage. These include energy arbitrage (i.e., buying electricity during low-price periods and selling it during high-price periods), balancing power to stabilize the network frequency, and congestion management. CBs accomodate all of these applications. In a future energy system, CBs could fill the gap between daily and seasonal storage (Jacob et al. 2023). Also, CBs provide a unique advantage: they can be thermally integrated, consuming low-temperature waste heat during charging. For example, Poletto et al. (2025) consider thermal integration of a data center with a Rankine-based CB, thereby reducing cooling demand by utilizing the data center's waste heat during charging.

Another advantage of CBs is that charging power, discharging power, and storage size can be chosen independently. At the same time, the resulting number of possible configurations makes finding a good CB design more challenging. This task is further complicated by the fact that a given design constrains how the CB can be operated. To address this challenge systematically, optimization is required. Furthermore, discrete decisions and accurate thermodynamics render the CB model non-convex, resulting in the existence of local minima. Optimization algorithms can be classified as either local or global, with the latter further divided into stochastic and deterministic methods (Locatelli and Schoen 2013). Only deterministic global optimization (DGO) can provide a guarantee that the best possible solution was found. Thus, DGO is preferable for design tasks of large-scale processes such as CBs.

Optimizing the CB design and operation requires embedding aspects such as fluid properties and heat transfer coefficients into the overall model. In many cases, calculation of these quantities is either handled by external libraries, which are not suitable for DGO, or the calculation procedure is so complex that directly embedding them into the model formulation would render the optimization intractable. Here, we replace such model components with data-driven surrogate models, resulting in a hybrid model (Psichogios and Ungar 1992; Kahrs and Marquardt 2007). We have extensively used this approach in the past to model ORCs by replacing thermodynamic calculations by artificial neural networks (ANNs) (e.g., Schweidtmann et al. 2019; Huster et al. 2020a; Huster et al. 2020b) and also recently for CBs working fluid (WF) screening (Lüthje et al. 2026).

The literature shows a gap between CB design optimization using accurate models, while assuming fixed operating characteristics, and CB design optimization within an energy systems modeling approach, using market information but not accurate CB models. Rech et al. (2025) optimize the round-trip efficiency (RTE) and energy density without consideration of the CB operation. Koksharov et al. (2024) minimize levelized cost of electricity (LCOE) while assuming a daily 4 h/4 h charging-discharging cycle. Tillmanns et al. (2022) minimize the specific investment cost (SIC), restricting the charging time to 8 h and the total cycle length to 24 h. Jacob et al. (2023) optimize the CB operation as part of a future energy systems scenario, considering a fixed CB design from literature. Nitsch et al. (2024) optimize storage size, charging power, discharging power and CB operation, also for a future energy systems scenario. However, they do not consider the influence of the RTE on CAPEX and assume linear cost correlations for the charging/discharging process and the TES. Allman et al. (2019) demonstrate how such a gap can be bridged by performing a so-called scheduling-informed design optimization of wind-powered ammonia production, in which they solve the optimal operation problem for multiple designs and then use the resulting data to train a surrogate model. Afterward, they solve the design optimization problem with the operation surrogate model embedded.

In this work, we extend our CB model (Lüthje et al. 2026) to optimize the design and operation of Rankine-based CBs. For this, we apply the approach of Allman et al. (2019) and define CB parameters that influence the operating behavior, repeatedly solve the optimal operation problem offline for different

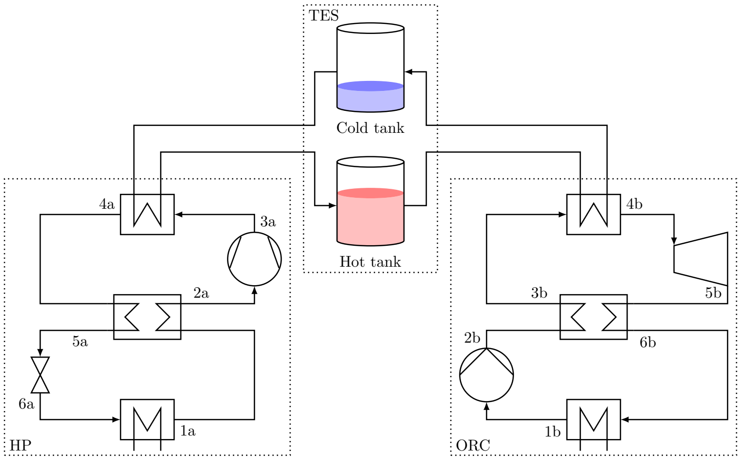

Figure 1: Flowsheet of the considered Rankine-based CB layout

parameters to generate data, and then embed a surrogate model that predicts the revenue from price arbitrage into the design optimization model. We use either ethylene oxide or cis-2-butene as the single WF for both HP and ORC, because they showed promising results in our previous work. We use the thermal oil Therminol-66 as storage medium. To maintain model accuracy, we use standard heat-exchange correlations, which we also solve offline and embed as surrogate models, thereby eliminating the need for wall temperatures as optimization variables.We optimize the model using the parallel version of our open-source deterministic global solver MAiNGO (Bongartz et al. 2018). Further, we implement reliability branching (Achterberg et al. 2005) to improve computational performance.

The article is structured as follows. First, we describe our CB model in Sec. 2, including the process description, the thermodynamics, the components, the used heat transfer correlations, the operation model, and the cost model. Next, we explain the proposed method in Sec. 3, which comprises data generation, ANN training, optimization procedure, implementation, and a description of the case study. Then, we investigate the results, including computational performance, in Sec. 4. Finally, we summarize our findings in Sec. 5.

2 Model

2.1 Process

In Fig. 1, we show a flowsheet of the CB we model and optimize in this work. We use a two-tank TES with Therminol 66 as storage medium. This storage configuration has the advantage that the operation of HP and ORC is independent of the state of charge (SoC). Therminol 66 matches the temperature range of Rankine-based CBs well and does not require to be stored under pressure

(Liang et al. 2022).

The charging process is a recuperated HP. Saturated, low-pressure vapor is preheated in the recuperator (1a → 2a). In the compressor, the charging power P_{el}^{+} is used to compress the WF to the high pressure level (2a → 3a). It then enters the main HP heat exchanger, where it is desuperheated, condensed, and subcooled, raising the storage medium from the low storage temperature to the high storage temperature in the process, thereby charging the CB (3a → 4a). Afterward, it passes through the other side of the recuperator and is further cooled down (4a → 5a) before being throttled into the two-phase region (5a → 6a). Finally, the WF is evaporated in the HP evaporator (6a → 1a).

The discharging process is a recuperated ORC. Saturated, low-pressure liquid is pumped to the high pressure level of the ORC (1b → 2b). It is then preheated in the ORC recuperator (2b → 3b). Next, the WF is further preheated, evaporated, and superheated in the main ORC heat exchanger (3b → 4b). The required heat is supplied by the storage medium, which is cooled down from the high storage temperature to the low storage temperature, thus discharging the CB. Subsequently, the WF is expanded to the low pressure level in the turbine, generating the discharging power P_{el}^{-} (4b → 5b). The WF then passes through the recuperator (5b → 6b) and the ORC condenser (6b → 1b), where it desuperheats and condenses completely.

Heat transfer from the HP and ORC to the environment is achieved via cooling water. We do not consider reversible turbomachinery (e.g., Torricelli et al. 2023) for the CB. Thus HP and ORC could also, in principle, use different WFs. A CB SoC of 0 %, or 100 % respectively, corresponds to the cold or hot storage tank being filled to maximum capacity.

2.2 Thermodynamics

2.2.1 Working fluids

We compute the required thermodynamic properties of the considered WFs via ANNs that take the thermodynamic state as an input. For example, we denote the ANN for calculating the (specific) entropy s_k of the thermodynamic state k with known pressure p_k and (specific) enthalpy h_k (assuming k is a vapor composed of WF i) as:

$$s_k = f_{p,h\rightarrow s}^{\mathrm{vap},\mathrm{ANN},i}\left(p_k, h_k\right)$$

Since we train separate ANNs for each phase, we implement constraints to ensure that the ANN inputs corresponds to the phase the ANN was trained on. For the example above, we impose a constraint ensuring that the input enthalpy exceeds the enthalpy of the saturated vapor at the same pressure.

$$h_k \geq f_{p\rightarrow h}^{\mathrm{sat\_vap},\mathrm{ANN},i}\left(p_k\right)$$

2.2.2 TES medium

In Modi and Pérez-Segarra (2014), the authors provide equations for thermodynamic properties of Therminol 66, fitted to the suppliers' datasheet. In addition to these equations, we fit the temperature as a function of the enthalpy via the following equation:

$$\frac{T\left(h\right)}{\mathrm{K}} = 308.68 \ln\left(6.1091 + \frac{h}{100\,\mathrm{kJ\,kg^{-1}}}\right) + 0.12745 \frac{h}{100\,\mathrm{kJ\,kg^{-1}}} - 2.6051$$

2.3 Rotating equipment

All rotating equipment (compressor, pump, and turbine) is modeled via its isentropic efficiency η_{is}, which we assume to be constant. First, we compute the enthalpy in the isentropic outlet state via either a liquid phase or vapor phase ANN depending on the output state.

$$h_{\text{is}}^{\text{out}} = f_{p,s\to h}^{\text{vap/liq,ANN},i}\left(p^{\text{out}}, s^{\text{in}}\right)$$

For the compressor and pump, the enthalpy of the real outflow is then given by

$$h^{\text{out}} = h^{\text{in}} + \frac{1}{\eta_{\text{is}}}\left(h_{\text{is}}^{\text{out}} - h^{\text{in}}\right)$$

and for the turbine by

$$h^{\text{out}} = h^{\text{in}} + \eta_{\text{is}}\left(h_{\text{is}}^{\text{out}} - h^{\text{in}}\right).$$

We can now compute the power drawn by the compressor and pump as

$$P = \dot{m}\left(h^{\text{out}} - h^{\text{in}}\right)$$

and the power provided by the turbine as

$$P = \dot{m}\left(h^{\text{in}} - h^{\text{out}}\right).$$

2.4 Heat exchangers

We model heat exchangers with an enthalpy balance, assuming isobaric operation and neglecting the heat transfer to the environment.

$$\dot{m}_{\text{cold}}\left(h_{\text{cold}}^{\text{out}} - h_{\text{cold}}^{\text{in}}\right) = \dot{m}_{\text{hot}}\left(h_{\text{hot}}^{\text{in}} - h_{\text{hot}}^{\text{out}}\right) = \dot{Q}$$

To compute capital costs, we determine the heat exchanger area based on the total heat duty, the total heat transfer coefficient U, and the logarithmic mean temperature difference (LMTD):

$$\begin{aligned} A =& \frac{\dot{Q}}{U\,\mathrm{LMTD}} \\ \mathrm{LMTD} =& \frac{\left(T_{\text{hot}}^{\text{out}} - T_{\text{cold}}^{\text{in}}\right) - \left(T_{\text{hot}}^{\text{in}} - T_{\text{cold}}^{\text{out}}\right)}{\ln\left(T_{\text{hot}}^{\text{out}} - T_{\text{cold}}^{\text{in}}\right) - \ln\left(T_{\text{hot}}^{\text{in}} - T_{\text{cold}}^{\text{out}}\right)} \end{aligned}$$

Table 1: Assumed geometry for shell and tube heat exchangers

Attribute	Variable	Value
Outer tube diameter	D_o	0.75 in
Tube sheet thickness	$D_\mathrm{o} - D_\mathrm{i}$	18 BWG
Tube pitch	L_p	1 in
Tube arrangement	-	triangular
Shell diameter	d_S	60 in
Baffle spacing	B	18 in
Number of tubes	n_t	3000

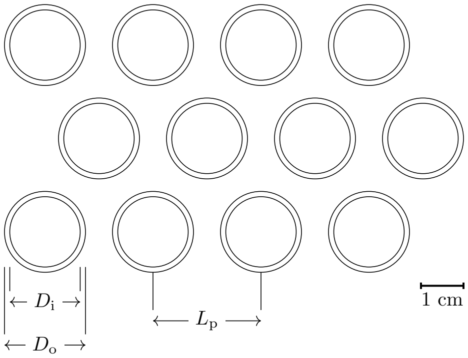

Figure 2: Sketch of the assumed tube bundle geometry

To this end, we require estimates of U. Literature provides heat transfer coefficient values for estimation purposes based on the phase of the two fluids (e.g., Turton et al. 2018). However, for this work, we require more precise values because heat exchanger costs constitute a large share of CAPEX. Further, we consider a wide range of pressures in our model. For a gas, pressure strongly influences the heat transfer coefficient. Thus, we perform standard heat transfer calculations, following the approach of Serth (2007). We assume that all heat exchangers are of shell-and-tube design. Further, we always place evaporation and condensation on the shell side. Therefore, we only need to consider single-phase flows on the tube side. As a rigorous optimization of the heat exchanger design (i.e., finding the optimal trade-off between heat transfer coefficient and pressure loss) exceeds the scope of this work, we assume a fixed geometry of the heat exchangers (cf. Tab. 1 and Fig. 2). For a fixed geometry and given flow states, the only remaining degree of freedom is the fluid velocity. We fix the fluid velocities for single-phase flows to 80 % of the maximum recommended velocities reported in literature as described below. Note that this contradicts the assumed fixed shell diameter and number of tubes, as these could be computed as a function of the total mass flow, density, fluid velocity, and tube cross-sectional area. However, shell diameter and number of tubes only moderately affect the shell-side heat transfer coefficients for boiling and condensation. The single-phase heat transfer correlations depend only on the inner and outer tube diameters and the tube pitch. Fixing the fluid velocities allows us to compute heat transfer coefficients for any given flows based only on the flow states. In particular, we can precompute the coefficients offline and embed them via surrogate models, more amenable to global optimization into the CB optimization model. In the following, we describe the calculation procedure we used to generate the data offline.

2.4.1 Single-phase on tube side

For the tube-side heat transfer, we require a correlation that covers both the transient and turbulent flow regimes. This is due to the high viscosity of Therminol 66 at low temperatures. Thus, we choose the Gnielinski equation (Serth 2007), neglecting the correction term for tube length and adding a viscosity correction term:

$$\mathrm{Nu} = \frac{0.125 f\,(\mathrm{Re} - 1000)\,\mathrm{Pr}}{1 + 12.7\sqrt{0.125 f}\left(\mathrm{Pr}^{\frac{2}{3}-1}\right)}\left(\frac{\mu}{\mu_{\mathrm{w}}}\right)^{0.14}$$

$$f = (0.782 \ln \mathrm{Re} - 1.51)^{-2}$$

Serth (2007) specifies the maximum tube velocity for water in carbon steel tubes $v_{\mathrm{cs,water}}^{\max}$ as $3.05\,\mathrm{m\,s^{-1}}$. For other liquids, the maximum velocity can be computed based on the fluid density.

$$v_{\mathrm{cs}}^{\max} = v_{\mathrm{cs,water}}^{\max}\sqrt{\frac{\rho_{\mathrm{water}}}{\rho}}$$

Serth (2007) also provides a formula for the maximum tube velocity for gases based on the pressure and molecular weight M.

$$v_{\mathrm{cs}}^{\max} = \frac{548.64\,\mathrm{m\,s^{-1}}}{\sqrt{pM0.145\,\mathrm{mol\,m\,s^2\,kg^{-2}}}}$$

2.4.2 Single-phase on shell side

Serth (2007) provides the following correlation for single-phase flows on the shell side (simplified Delaware method):

$$\begin{aligned}\mathrm{Nu} &= j_{\mathrm{H}}\mathrm{Pr}^{\frac{1}{3}}\left(\frac{\mu}{\mu_{\mathrm{w}}}\right)^{0.14}\\ j_{\mathrm{H}} &= 0.5\left(1+\frac{B}{d_{\mathrm{S}}}\right)\left(0.08\mathrm{Re}^{0.6821}+0.7\mathrm{Re}^{0.1772}\right)\end{aligned}$$

According to Serth (2007), the baffle spacing B should be in the range of 20 % to 40 % of the shell diameter d_{S}. We assume $B/d_{\mathrm{S}} = 30\,\%$. Towler and Sinnott (2013) state the maximum shell-side velocity for liquids to be $v^{\max} = 1\,\mathrm{m\,s^{-1}}$. For the maximum shell-side velocity of vapors, we use the pressure and molar mass dependent correlation of Bahadori and Vuthaluru (2010). This correlation was fitted to data provided by Ludwig (2001), which do not cover pressures below 0.5 bar. Thus, for all pressures below 0.5 bar, we evaluate the correlation at $p = 0.5\,\mathrm{bar}$.

2.4.3 Boiling on shell side

The heat transfer coefficient for a boiling fluid on horizontal tubes can be determined with the Mostinski correlation:

$$\begin{aligned}h_{\mathrm{nb}} &= 1.167\times10^{-8}\,\mathrm{W\,m^{-2}\,K^{-1}}\left(\frac{p_{\mathrm{crit}}}{\mathrm{kPa}}\right)^{2.3}\left(\frac{\Delta T_{\mathrm{e}}}{\mathrm{K}}\right)^{2.333}{F_{\mathrm{P}}}^{3.333}\\ F_{\mathrm{P}} &= 1.8\left(\frac{p}{p_{\mathrm{crit}}}\right)^{0.17}+4\left(\frac{p}{p_{\mathrm{crit}}}\right)^{1.2}+10\left(\frac{p}{p_{\mathrm{crit}}}\right)^{10}\end{aligned}$$

The temperature difference ΔT_{e} is the difference between the wall temperature and the boiling temperature. The effect of the tube bundle is accounted for by the factor F_{b} and the heat transfer coefficient for natural convection h_{nc}. Serth (2007) recommends using $h_{\mathrm{nc}} = 250\,\mathrm{W\,m^{-2}\,K^{-1}}$ as a rough estimate.

$$\begin{aligned}h_{\mathrm{b}} &= h_{\mathrm{nb}}F_{\mathrm{b}} + h_{\mathrm{nc}}\\ F_{\mathrm{b}} &= 1 + 0.1\left(\frac{0.785D_{\mathrm{b}}D_{\mathrm{o}}}{0.866{L_{\mathrm{p}}}^2}-1\right)^{0.75}\end{aligned}$$

We select the tube bundle diameter based on Thulukkanam (2013):

$$D_{\mathrm{b}} = d_{\mathrm{S}} - \left(0.005\,\mathrm{m} + \frac{0.012\,\mathrm{m}^2}{d_{\mathrm{S}}}\right)$$

2.5 Condensation on shell side

The heat transfer coefficient of condensation on the outside of a single horizontal tube can be computed as:

$$h = 0.728\,\mathrm{W\,m^{-2}\,K^{-1}} \left(\frac{k_\mathrm{L}^3 \rho_\mathrm{L} \left(\rho_\mathrm{L} - \rho_\mathrm{V}\right) g \Delta h_\mathrm{c}}{\mu_\mathrm{L} \Delta T_\mathrm{c} D_\mathrm{o}} \right)^{\frac{1}{4}}$$

In this equation, g is the gravitational acceleration, Δh_c is the condensation enthalpy, and ΔT_c is the difference between wall temperature and condensing temperature. The effect of the tube bundle can be estimated based on the number of tubes n_t with:

$$h_\mathrm{tb} = h\, n_\mathrm{t}^{-\frac{1}{9}}$$

2.5.1 Overall heat transfer coefficient

Calculating the overall heat transfer coefficient requires determining the wall temperature T_w as the shell- and tube-side heat transfer coefficients depend on it. Assuming that the diffusive heat transfer inside the heat exchanger construction material is much faster than the convective heat transfer, i.e., $k \gg h_\mathrm{t}$, $k \gg h_\mathrm{s}$, we can solve the following energy balance for T_w:

$$h_\mathrm{t}(T_\mathrm{w})\left(T_\mathrm{t} - T_\mathrm{w}\right) = h_\mathrm{s}(T_\mathrm{w})\left(T_\mathrm{w} - T_\mathrm{s}\right)$$

The overall heat transfer coefficient U_c for a clean heat exchanger is then given by:

$$\frac{1}{U_\mathrm{c}} = \frac{D_\mathrm{o}}{h_\mathrm{t} D_\mathrm{i}} + \frac{D_\mathrm{o} \ln \frac{D_\mathrm{o}}{D_\mathrm{i}}}{2k} + \frac{1}{h_\mathrm{s}}$$

Additionally, we consider fouling by adding fouling factors taken from Turton et al. (2018) ($h_\mathrm{fo} = h_\mathrm{fi} = 5675\,\mathrm{W\,m^{-2}\,K^{-1}}$) to compute the dirty heat transfer coefficient U_d:

$$\frac{1}{U_\mathrm{d}} = \frac{1}{U_\mathrm{c}} + \frac{D_\mathrm{i}}{D_\mathrm{o}} \frac{1}{h_\mathrm{fo}} + \frac{1}{h_\mathrm{fi}}$$

2.5.2 Recuperators

The recuperators exchange heat between a low pressure gaseous stream and a high pressure liquid stream. The general recommendation is to place the higher pressure stream on the tube side to reduce capital costs (e.g., Serth 2007). However, the low pressure (and thus low density) of the gaseous stream results in low heat transfer coefficients when placed on the shell side. Thus, we place the recuperator vapor stream on the tube side, accepting the increased capital cost in exchange for a higher heat transfer coefficient.

2.6 Thermal energy storage

We assume isobaric operation for both WF and storage medium in the TES heat exchangers. When hot and cold storage medium temperature ($T_{\text{TES}}^{\text{hot}}$, $T_{\text{TES}}^{\text{cold}}$), the HP WF mass flow $\dot{m}_{\text{HP}}$, and the state of the WF at the inlet and outlet are given, we can calculate the mass flow rate of the ORC WF based on the assumption of negligible heat loss to the environment.

$$\dot{m}_{\text{ORC}} = \dot{m}_{\text{HP}} \frac{h_{\text{HP}}^{\text{in}} - h_{\text{HP}}^{\text{out}}}{h_{\text{ORC}}^{\text{out}} - h_{\text{ORC}}^{\text{in}}} r$$

Here, we consider the battery parameter r (the ratio of the maximum charging time to the maximum discharging time). Next, we compute the storage medium flow rates for the charging and discharging processes.

$$\dot{m}_{\text{TES}}^{\text{HP}} = \dot{m}_{\text{HP}} \frac{h_{\text{HP}}^{\text{in}} - h_{\text{HP}}^{\text{out}}}{h_{\text{TES}}^{\text{hot}} - h_{\text{TES}}^{\text{cold}}}$$

$$\dot{m}_{\text{TES}}^{\text{ORC}} = \dot{m}_{\text{ORC}} \frac{h_{\text{ORC}}^{\text{out}} - h_{\text{ORC}}^{\text{in}}}{h_{\text{TES}}^{\text{hot}} - h_{\text{TES}}^{\text{cold}}}$$

Using the flow rates of the storage medium, we can determine the temperatures of the WF and the storage medium at any point in the TES heat exchanger. We add constraints to enforce minimum temperature differences between the WF and the storage medium at the heat exchanger inlet and outlet, as well as at the saturated states of the WF. Under the assumption of constant heat capacities, this would be sufficient to guarantee the minimum temperature difference throughout the TES heat exchanger. However, both WF and TES do not have a constant heat capacity, and we observe a violation of the minimum temperature difference when constraints are imposed exclusively at the points described above. To address this issue without increasing the model complexity, we implement a single additional discretization point slightly above the saturated vapor state for the HP WF and slightly below the saturated liquid state for the ORC WF.

$$T_{\text{HP}} \left(0.95 h_{\text{HP}}^{''} + 0.05 h_{\text{HP}}^{\text{in}}\right) \geq T_{\text{TES}}^{\text{HP}} \left(0.95 h_{\text{HP}}^{''} + 0.05 h_{\text{HP}}^{\text{in}}\right) + \Delta T^{\min}$$

$$T_{\text{ORC}} \left(0.9 h_{\text{ORC}}^{'} + 0.1 h_{\text{ORC}}^{\text{in}}\right) + \Delta T^{\min} \leq T_{\text{TES}}^{\text{ORC}} \left(0.9 h_{\text{ORC}}^{'} + 0.1 h_{\text{ORC}}^{\text{in}}\right)$$

We then compute the required amount of storage medium:

$$m_{\text{TES}} = \dot{m}_{\text{TES}}^{\text{HP}} t_{\max}^{+}$$

For the tank volume, we assume that the fill level varies between 0 % to 100 % during operation of the CB.

$$V_{\text{tank}}^{\text{hot}} = \frac{m_{\text{TES}}}{\rho_{\text{TES}} \left(T_{\text{TES}}^{\text{hot}}\right)}$$

$$V_{\text{tank}}^{\text{cold}} = \frac{m_{\text{TES}}}{\rho_{\text{TES}} \left(T_{\text{TES}}^{\text{cold}}\right)}$$

2.7 Optimal operation

To optimize the operation of the CB, we make the following assumptions:

- We neglect the heat loss of the TES to the environment. This is a reasonable assumption, as the tanks are large and can be easily insulated. Benato and Stoppato (2018) specify a self-discharge rate of $1\,\%\,\mathrm{d}^{-1}$.
- We neglect ramping constraints, motivated by the time discretization of 1 h. Furthermore, determining ramp rates would require a detailed dynamic model of the CB and its components, which is beyond the scope of this work.
- We neglect efficiency losses due to off-nominal operation. While part-load behavior is an open research question for CBs (Liang et al. 2022), for most of the operation period, the CB will either charge/discharge at nominal power or do nothing due to the previous assumptions. Thus, the influence of off-design efficiency losses is negligible.
- Further, we neglect the influence of the fluctuations in the ambient temperature on the RTE. It follows that the CB is always operating at a constant RTE.
- We assume that the CB operation does not influence the market clearing (i.e., the CB is a price taker) due to its small relative size ($\approx 0.1\,\%$ of the volume traded on the German day-ahead market).

With the assumption of constant RTE, no ramping constraints, and a given nominal charging power, only 3 aspects of the design influence the operation: the size of the storage (how much energy can be stored); the RTE (how much of the stored energy is available for discharging); and the size of the discharging process (how fast can the stored energy be discharged). For the operation model, we choose the following 3 parameters to describe the CB operation characteristics:

1. RTE $\eta_{\mathrm{rt}} = \frac{P^{-}_{\mathrm{el,nom}} t^{-}_{\mathrm{max}}}{P^{+}_{\mathrm{el,nom}} t^{+}_{\mathrm{max}}}$. This parameter only depends on the thermodynamic trajectory of WF and storage medium, and is thus independent of the sizing of the CB.
2. Maximum charging time t^{+}_{max}. For given thermodynamic trajectories of HP and TES, this parameter only affects the amount of storage medium and the size of the storage tanks.
3. Ratio between maximum charging and discharging time $r = t^{+}_{\mathrm{max}}/t^{-}_{\mathrm{max}} = \dot{Q}^{-}_{\mathrm{nom}}/\dot{Q}^{+}_{\mathrm{nom}}$. For given thermodynamic trajectories of HP and ORC, this parameter only affects the sizing of the ORC components. It is independent of the TES.

While many other parameter sets exist, we choose this one because it provides a straightforward description of the characteristics of the CB operation. Also, these parameters are independent of the nominal charging power. We now set up a simple mixed-integer linear program (MILP) battery operation model (eqs. 1-6) for a CB that buys and sells electricity on the spot market.

$$
\begin{aligned}
\min_{\boldsymbol{P}_{\mathrm{el}}^{+},\boldsymbol{P}_{\mathrm{el}}^{-},\boldsymbol{s},\boldsymbol{y}} \quad & \sum_{t}^{T} c_{\mathrm{elec},t}\left(P_{\mathrm{el},t}^{+} - P_{\mathrm{el},t}^{-}\right)\Delta t && && (1)\\
\text{s.t.} \quad & 0 \leq P_{\mathrm{el},t}^{+} \leq y_t P_{\mathrm{el,nom}}^{+} && \forall t \in \{1,\dots,T\} && (2)\\
& 0 \leq P_{\mathrm{el},t}^{-} \leq (1-y_t)\, r\, \eta_{\mathrm{rt}}\, P_{\mathrm{el,nom}}^{+} && \forall t \in \{1,\dots,T\} && (3)\\
& s_{t+1} = s_t + \frac{\Delta t}{P_{\mathrm{el,nom}}^{+} t_{\max}^{+}}\left(P_{\mathrm{el},t}^{+} - \frac{P_{\mathrm{el},t}^{-}}{\eta_{\mathrm{rt}}}\right) && \forall t \in \{1,\dots,T\} && (4)\\
& s_1 = s_{T+1} = 0.5 && && (5)\\
& P_{\mathrm{el},t}^{+}, P_{\mathrm{el},t}^{-} \in \mathbb{R}, s_t \in [0,1] \subset \mathbb{R}, y_t \in \{0,1\} && \forall t \in \{1,\dots,T\} && (6)
\end{aligned}
$$

This model is inspired by the generalized flexible process model proposed by Schäfer et al. (2020) and implements the charging and discharging as two different operating modes (Basán et al. 2018) via the binary variable y_t. We note that one could drop y_t for time periods in which the electricity price $c_{\mathrm{elec},t}$ is nonnegative. In these periods, simultaneously charging and discharging (which is prevented by y_t) will never be optimal due to $\eta_{\mathrm{rt}} < 1$. We assume that the charge level of the CB s_t is at 50 % at the start and end of the considered operation interval.

As an option to improve economics, we extend the operation model to include further revenue streams. To this end, we focus on additionally providing a small fraction of the nominal power as primary response as one of the core applications of electricity storage (Schmidt et al. 2019). In Germany, frequency containment reserve (FCR) is provided in 4 h blocks, during which the control reserve has to be at full capacity in both directions within 30 s (50Hertz et al. 2026). In contrast to the other types of frequency reserves, for FCR there is only a capacity market, and only the provision of the capacity is reimbursed. FCR can only be offered in steps of 1 MW.

In a previous work, our group investigated bidding strategies for the German FCR market (Schäfer et al. 2019). Since the remuneration scheme in German markets recently changed from pay-as-bid to pay-as-clear, the model can be significantly simplified: We can neglect bidding strategies and assume the CB to be an FCR price taker (similar to the day-ahead market). The discrete nature of the FCR capacity and the constraints ensuring the availability of the FCR capacity at all times remain unaffected. For our operation model with FCR, we make the following assumptions:

- No mode switching (e.g., switching from charging to discharging) may occur during a 4 h-block in which FCR is provided. This prevents the worst-case scenario in which FCR is retrieved exactly when the HP shuts down and ORC starts up (or vice-versa).

- We assume that the influence of the actual delivered FCR on the operating schedule (when to charge/discharge at which power) of the CB can be neglected. This is motivated by several factors. FCR is retrieved proportionally to the grid frequency deviation, with the full capacity only being retrieved at a deviation of $0.2\,\mathrm{s}^{-1}$. Also, the maximum retrieval period is limited to 15 min after which other means of frequency containment take over. Thus, the amount of FCR actually provided is small compared to the reserved capacity. Also, FCR is retrieved in both directions so that subsequent retrieval periods can cancel each other out.
- We assume that HP and ORC can provide 10 % of their nominal power as FCR ($P^{+}_{\mathrm{FCR,max}} = 0.1\,P^{+}_{\mathrm{el,nom}}$ and $P^{-}_{\mathrm{FCR,max}} = 0.1\,P^{-}_{\mathrm{el,nom}}$). Again, determining the largest physically feasible FCR provision would require a more detailed model. We expect the heat exchangers to be the limiting factor due to thermal stresses. Thus, we take 10 % of the nominal power as a conservative estimate.

With these assumptions, we can extend the CB operation model (eqs. 1-6) in the following way:

$$
\begin{aligned}
\min_{\substack{\boldsymbol{P}^{+}_{\mathrm{el}},\boldsymbol{P}^{-}_{\mathrm{el}},\boldsymbol{s},\boldsymbol{y},\\ \boldsymbol{P}^{+}_{\mathrm{FCR}},\boldsymbol{P}^{-}_{\mathrm{FCR}}}} \quad & \sum_{t}^{T} c_{\mathrm{elec},t}\left(P^{+}_{\mathrm{el},t} - P^{-}_{\mathrm{el},t}\right)\Delta t + \sum_{t^*}^{\lceil \frac{T}{4} \rceil} c_{\mathrm{FCR},t^*}\left(P^{+}_{\mathrm{FCR},t^*} + P^{-}_{\mathrm{FCR},t^*}\right) \\
\text{s.t.} \quad & P^{+}_{\mathrm{FCR},\lceil \frac{t}{4} \rceil} \le P^{+}_{\mathrm{el},t} \le y_t P^{+}_{\mathrm{el,nom}} - P^{+}_{\mathrm{FCR},\lceil \frac{t}{4} \rceil} && \forall t \in \{1,\dots,T\} \\
& P^{-}_{\mathrm{FCR},\lceil \frac{t}{4} \rceil} \le P^{-}_{\mathrm{el},t} \le (1-y_t)\,P^{-}_{\mathrm{el,nom}} - P^{-}_{\mathrm{FCR},\lceil \frac{t}{4} \rceil} && \forall t \in \{1,\dots,T\} \\
& 0 \le P^{+}_{\mathrm{FCR},\lceil \frac{t}{4} \rceil} \le y_t P^{+}_{\mathrm{FCR,max}} && \forall t \in \{1,\dots,T\} \\
& 0 \le P^{-}_{\mathrm{FCR},\lceil \frac{t}{4} \rceil} \le (1-y_t)\,P^{-}_{\mathrm{FCR,max}} && \forall t \in \{1,\dots,T\} \\
& s_{t+1} = s_t + \frac{P^{+}_{\mathrm{el},t}\Delta t}{P^{+}_{\mathrm{el,nom}} t^{+}_{\max}} - \frac{P^{-}_{\mathrm{el},t}\Delta t}{P^{-}_{\mathrm{el,nom}} t^{-}_{\max}} && \forall t \in \{1,\dots,T\} \\
& s_1 = s_{T+1} = 0.5 \\
& P^{+}_{\mathrm{el},t}, P^{-}_{\mathrm{el},t} \in \mathbb{R},\, s_t \in [0,1] \subset \mathbb{R},\, y_t \in \{0,1\} && \forall t \in \{1,\dots,T\} \\
& P^{+}_{\mathrm{FCR},t^*}, P^{-}_{\mathrm{FCR},t^*} \in \mathbb{N}_0 && \forall t^* \in \{1,\dots,\lceil T/4 \rceil\}
\end{aligned}
$$

Note that the unit of all electrical powers is MW as the FCR capacity can only be chosen in steps of 1 MW. We use the ceiling function $\lceil \frac{t}{4} \rceil$ to indicate the mapping of the 1 h-blocks of day-ahead prices to the 4 h-blocks in which FCR is provided.

2.8 Cost calculation

All used cost correlations are taken from Turton et al. (2018), as they are widely used and depend only on component size. For the considered CB size, this leads to extrapolation for some components. We assume all components are constructed from carbon steel.

We calculate the total module cost from the bare module cost of the individual components (Turton et al. 2018):

$$C_{\mathrm{TM}} = 1.18 \sum C_{\mathrm{BM},i}$$

We then calculate the grassroots cost C_{GR}:

$$C_{\mathrm{GR}} = C_{\mathrm{TM}} + 0.5 \sum C^0_{\mathrm{BM},i}$$

with

$$\begin{aligned} C_{\mathrm{BM},i} &= C^0_{\mathrm{p},i} \left(B_1 + B_2 F_{\mathrm{P}} F_{\mathrm{M}}\right) \\ C^0_{\mathrm{BM},i} &= C^0_{\mathrm{p},i} \left(B_1 + B_2 F^0_{\mathrm{P}} F^0_{\mathrm{M}}\right) \end{aligned}$$

$C^0_{\mathrm{p},i}$ and F_{P} are Guthrie cost functions for which we apply the envelopes we proposed in Najman et al. (2019). The capital recovery factor CRF for an interest rate f_{i} over y years is defined as:

$$\mathrm{CRF} = \frac{(1 + f_{\mathrm{i}})^y f_{\mathrm{i}}}{(1 + f_{\mathrm{i}})^y - 1}.$$

Thus, we can determine the CAPEX C_{Cap}:

$$C_{\mathrm{Cap}} = \mathrm{CRF} \times C_{\mathrm{GR}} \tag{7}$$

For the turbine, special consideration is required. The cost correlation given in Turton et al. (2018) extrapolates poorly (costs decrease with increasing shaft power). Thus, we determine the slope at the maximum turbine size according to the source and extrapolate linearly.

In addition to component costs, we also consider the cost of the storage medium. In Zhao et al. (2022), the cost of Therminol 66 is given as $1\,\$\,\mathrm{kg}^{-1}$. We assume that the storage medium does not need to be replaced within the CB lifetime.

3 Method

3.1 Data generation

3.1.1 Thermodynamics

We define a maximum temperature $T^{\max}$ which must not be exceeded by the WF in the CB process. This constrains the HP compressor outlet temperature, which is the hottest state in the process. We set this maximum temperature to 750 K based on the maximum compressor outlet temperature given in Dumont et al. (2020). If the equation of state (EoS), that is implemented in the

Table 2: Bounds for data generation of thermodynamic data

Variable	Bounds
p	$[0.1\,\mathrm{bar}, 0.9\,p_{\mathrm{crit}}]$
T	$[250\,\mathrm{K}, T^{\max}]$

Table 3: Heat exchanger data inputs

Process	Type	Variables
HP	Recuperator	$T^{\mathrm{l}}_{\mathrm{WF}},\ T^{\mathrm{v}}_{\mathrm{WF}},\ p^{\mathrm{v}}_{\mathrm{WF}}$
	Desuperheater	$T_{\mathrm{TES}},\ T_{\mathrm{WF}}$
	Condenser	$T_{\mathrm{TES}},\ p_{\mathrm{WF}}$
	Subcooler	$T_{\mathrm{TES}},\ T_{\mathrm{WF}},\ p_{\mathrm{WF}}$
	Ambient evaporator	$T_{\mathrm{amb}},\ p_{\mathrm{WF}}$
ORC	Recuperator	$T^{\mathrm{l}}_{\mathrm{WF}},\ T^{\mathrm{v}}_{\mathrm{WF}},\ p^{\mathrm{v}}_{\mathrm{WF}}$
	Superheater	$T_{\mathrm{TES}},\ T_{\mathrm{WF}}$
	Evaporator	$T_{\mathrm{TES}},\ p_{\mathrm{WF}}$
	Preheater	$T_{\mathrm{TES}},\ T_{\mathrm{WF}},\ p_{\mathrm{WF}}$
	Ambient desuperheater	$T_{\mathrm{amb}},\ T_{\mathrm{WF}},\ p_{\mathrm{WF}}$
	Ambient condenser	$T_{\mathrm{amb}},\ p_{\mathrm{WF}}$

thermodynamic library, does not support this temperature, we set $T^{\max}$ to the maximum temperature supported by the EoS instead. For the data generation, we only need to sample data up to $T^{\max}$. We summarize the bounds used for the thermodynamic data generation in Tab. 2. We generate 10 000 data points of pressure and temperature using latin hypercube sampling (LHS) within these bounds, forming our initial dataset D. Then, we split the dataset into the liquid and the gaseous phase:

$$
\begin{aligned}
D_{\mathrm{vap}} &= \{(p, T) \in D \mid T \geq T_{\mathrm{sat}}(p)\} \\
D_{\mathrm{liq}} &= \{(p, T) \in D \mid T < T_{\mathrm{sat}}(p)\}
\end{aligned}
$$

For every data point, we use the thermodynamic library to compute the corresponding enthalpy and entropy.

To obtain the dataset for the saturated states, we sample 1000 points within the pressure bounds. For these points, we compute the temperature, liquid and vapor enthalpies, and liquid and vapor entropies.

3.1.2 Heat exchanger

Given the fixed heat exchanger geometry and flow velocities, we can compute heat transfer coefficients based only on the average flow conditions on both sides of the heat exchanger. Furthermore, we neglect the influence of the liquid-flow pressure on the properties of the liquid flow and thus on the heat transfer

Table 4: Bounds for data generation of operational revenue

Variable	Bounds
η_{rt}	$[0.1, 0.6]$
$t^+_{\max}$	$[4\,\mathrm{h}, 24\,\mathrm{h}]$
$r = t^+_{\max}/t^-_{\max}$	$[0.5, 2]$

coefficients. This leaves us with the variables summarized in Tab. 3. We generate 10 000 data points for every heat exchanger type using LHS. Then, we filter inconsistent data points (e.g., $T^{\mathrm{v}}_{\mathrm{WF}} < T_{\mathrm{sat}}(p^{\mathrm{v}}_{\mathrm{WF}})$). Next, we solve for the wall temperature T_{w} and compute the clean heat transfer coefficient U_{c} for every remaining data point. We repeat this process for the two considered WFs, resulting in two separate sets of heat transfer ANNs.

3.1.3 Operation

We use LHS to sample 5000 data points for the three battery parameters within the bounds shown in Tab. 4. In our previous work, we demonstrated that a CB with the structure we consider can achieve an RTE of up to 60 %. This motivates our choice for the upper bound of the RTE. For the lower bound, we select an arbitrary value of 10 %. The bounds on the maximum charging time $t^+_{\max}$ and the charging time ratio r cover a majority of previously proposed CB concepts (Liang et al. 2022; Vecchi et al. 2022).

We solve the optimal operation problem for each set of battery parameters (each data point) over an entire year, yielding the optimal yearly operational revenue achievable with a CB with these parameters. We repeat the process for all considered price profiles. For the electricity cost, we use data from the German day-ahead market (Bundesnetzagentur 2024). Additionally, we generate data for the optimal revenues when also providing FCR. The prices for FCR are published in 50Hertz et al. (2026).

The optimal operation problem with FCR is challenging to solve for some battery parameters. Thus, we switch the MILP solver strategy to only improve the best feasible solution after 60 s and stop the run after 120 s.

3.2 ANN training

We train ANNs to predict WF thermodynamics, heat transfer coefficients, and operational revenue. Following the approach of Schweidtmann et al. (2019), we train a separate ANN for every input-output function required by the model. As a consequence, for a single WF, multiple ANNs have to be trained for the property prediction as shown in Tab. 5. While this is not inherently required, we additionally train an ANN for the evaporation enthalpy Δh_{evap}, which we use instead of the difference between the ANNs for saturated vapor and liquid enthalpies, as we expect this to result in a model formulation that is better suited for DGO. Also, we train the ANNs for the heat transfer coefficients on the inverse of the clean heat transfer coefficient $1/U_{\mathrm{c}}$, avoiding a division operation in the model.

Table 5: Overview of trained ANNs for predicting thermodynamic properties of a single WF

Phase	**Inputs**	**Output**
Vapor	p, h	T
	p, T	h
	p, h	s
	p, s	h
Liquid	p, h	T
	p, s	h
Saturated	p	T
	p	$h^{'}$
	p	$h^{''}$
	p	$s^{'}$
	p	Δh_{evap}

DGO requires convex and concave relaxations (over-/underestimators) of the objective function and constraints. MAiNGO uses the McCormick technique (McCormick 1976) to construct these relaxations. Prior publications (e.g., Najman et al. (2019)) have shown that tightening these relaxations (i.e., reducing the distance between convex and concave relaxations) can significantly improve computational performance. For ANNs, envelopes (the tightest possible relaxations) exist for the activation function (Schweidtmann et al. 2019). However, the ANNs are a composition of multiple activation functions, the relaxation of which can vary in tightness. Thus, for the ANN training, we follow the approach of our previous work (Lüthje et al. 2026). In short, the training starts with a small initial ANN size. The ANN size is increased until a previously specified target mean squared error (MSE) is reached. We repeat this procedure n times, resulting in n different ANNs that all reach the target MSE. Of these ANNs we select the one with the tightest McCormick relaxations (i.e., the smallest average distance between convex and concave relaxation) over the training data range.

Before training, we normalize the data so that the inputs are within the range $[-1, 1]$ and the output has a mean of 0 and a standard deviation of 1. We select a target MSE of 1×10^{-4} for all ANNs used in the model. Training of the ANNs for thermodynamics and heat transfer coefficients is repeated $n = 5$ times. We repeat the training of ANNs for the revenue $n = 10$ times, as only 1 ANN needs to be trained for each price profile and as we expect these ANNs to have a large influence on the computational performance.

3.3 Optimization

Instead of combining CAPEX and revenue into a single objective function, we consider a bi-objective optimization minimizing CAPEX (C_{Cap}, eq. 7) and maximizing revenue (R). Without using a surrogate model for the optimal operational revenue, we would need to solve a combined operation and design optimization problem:

$$\begin{aligned}\min_{\boldsymbol{x}\in\mathbb{R}^{n_x},\boldsymbol{y}\in\mathbb{R}^{n_y},\boldsymbol{z}\in\mathbb{N}_0^{n_z}} \quad & \left(C_{\text{Cap}}\left(\boldsymbol{x}\right), -R\left(\boldsymbol{x},\boldsymbol{y},\boldsymbol{z}\right)\right)\\ \text{s.t.} \quad & \boldsymbol{h}_{\text{Design}}\left(\boldsymbol{x}\right)=\boldsymbol{0}\\ & \boldsymbol{h}_{\text{Operation}}\left(\boldsymbol{x},\boldsymbol{y},\boldsymbol{z}\right)=\boldsymbol{0}\\ & \boldsymbol{g}_{\text{Design}}\left(\boldsymbol{x}\right)\leq\boldsymbol{0}\\ & \boldsymbol{g}_{\text{Operation}}\left(\boldsymbol{x},\boldsymbol{y},\boldsymbol{z}\right)\leq\boldsymbol{0}.\end{aligned}$$

This problem is large because optimal values for the design variables $\boldsymbol{x}$, the continuous operation variables $\boldsymbol{y}$, and the discrete operation variables $\boldsymbol{z}$ must be determined simultaneously. We solve the optimal operation problem for fixed design variables and train a surrogate model for it.

$$\begin{aligned}R_{\text{ANN}}\left(\boldsymbol{x}\right)\approx-\min_{\boldsymbol{y}\in\mathbb{R}^{n_y},\boldsymbol{z}\in\mathbb{N}_0^{n_z}} \quad & -R\left(\boldsymbol{x},\boldsymbol{y},\boldsymbol{z}\right)\\ \text{s.t.} \quad & \boldsymbol{h}_{\text{Operation}}\left(\boldsymbol{x},\boldsymbol{y},\boldsymbol{z}\right)=\boldsymbol{0}\\ & \boldsymbol{g}_{\text{Operation}}\left(\boldsymbol{x},\boldsymbol{y},\boldsymbol{z}\right)\leq\boldsymbol{0}.\end{aligned}$$

Note that the effort required for obtaining the exact parametric solution of the optimal operation problem can, in the worst case, scale exponentially with the problem size (Murty 1980). Thus, in theory, the data requirement can also scale exponentially. However, in practice, learning the optimal objective of scheduling problems works well (Dias and Ierapetritou 2020; Ikonen et al. 2025).

Embedding the surrogate model $R_{\text{ANN}}\left(\boldsymbol{x}\right)$ results in the following operation-aware design optimization problem:

$$\begin{aligned}\min_{\boldsymbol{x}\in\mathbb{R}^{n_x}} \quad & \left(C_{\text{Cap}}\left(\boldsymbol{x}\right), -R_{\text{ANN}}\left(\boldsymbol{x}\right)\right)\\ \text{s.t.} \quad & \boldsymbol{h}_{\text{Design}}\left(\boldsymbol{x}\right)=\boldsymbol{0}\\ & \boldsymbol{g}_{\text{Design}}\left(\boldsymbol{x}\right)\leq\boldsymbol{0}.\end{aligned}$$

We apply the ϵ-constraint method to compute the Pareto front. To this end, we choose the revenue as the primary objective and discretize CAPEX. This has the advantage that, for a given WF pair, the minimum CAPEX and the CAPEX at the maximum revenue are independent of the considered price profile. Thus, we can use the same CAPEX discretization regardless of the operating year. We can then compare the most cost-effective CB across different operational models for a given maximum CAPEX, highlighting differences in investment decisions based on the operating year considered. Thus, we solve multiple instances of a

Table 6: Optimization variables and their bounds. We denote the lower and upper bounds of the optimization variable x by x^{LB} and x^{UB}, respectively.

Variable	Lower bound	Upper bound
$p_{\mathrm{L}}^{\mathrm{HP}}$	$0.2\,\mathrm{bar}$	$p_{\mathrm{sat}}^{\mathrm{HP}}\left(T_{\mathrm{amb}} - \Delta T_{\mathrm{amb}} - \Delta T_{\mathrm{HEX,amb}}^{\mathrm{min}}\right)$
$p_{\mathrm{H}}^{\mathrm{HP}}$	$0.4\,p_{\mathrm{crit}}^{\mathrm{HP}}$	$0.8\,p_{\mathrm{crit}}^{\mathrm{HP}}$
$p_{\mathrm{L}}^{\mathrm{ORC}}$	$p_{\mathrm{sat}}^{\mathrm{ORC}}\left(T_{\mathrm{amb}} + \Delta T_{\mathrm{HEX,amb}}^{\mathrm{min}}\right)$	$p_{\mathrm{sat}}^{\mathrm{ORC}}\left(T_{\mathrm{amb}} + 30\,\mathrm{K}\right)$
$p_{\mathrm{H}}^{\mathrm{ORC}}$	$0.4\,p_{\mathrm{crit}}^{\mathrm{ORC}}$	$0.8\,p_{\mathrm{crit}}^{\mathrm{ORC}}$
$\Delta h_{\mathrm{recup}}^{\mathrm{HP}}$	$0.01\,\Delta h_{\mathrm{recup}}^{\mathrm{HP,UB}}$	$h'\left(p_{\mathrm{H}}^{\mathrm{HP,UB}}\right) - h'\left(p_{\mathrm{L}}^{\mathrm{HP,LB}}\right)$
$\Delta h_{\mathrm{recup}}^{\mathrm{ORC}}$	$0.01\,\Delta h_{\mathrm{recup}}^{\mathrm{ORC,UB}}$	$h'\left(p_{\mathrm{H}}^{\mathrm{ORC,UB}}\right) - h'\left(p_{\mathrm{L}}^{\mathrm{ORC,LB}}\right)$
$\Delta h_{\mathrm{TES}}^{\mathrm{HP}}$	$\Delta h_{\mathrm{evap}}^{\mathrm{HP}}\left(p_{\mathrm{H}}^{\mathrm{HP,UB}}\right)$	$h_{v}^{\mathrm{HP}}\left(p_{\mathrm{H}}^{\mathrm{HP,LB}}, T^{\mathrm{max}}\right) - h'\left(p_{\mathrm{L}}^{\mathrm{HP,LB}}\right)$
$\Delta h_{\mathrm{TES}}^{\mathrm{ORC}}$	$\Delta h_{\mathrm{evap}}^{\mathrm{ORC}}\left(p_{\mathrm{H}}^{\mathrm{ORC,UB}}\right)$	$h_{v}^{\mathrm{ORC}}\left(p_{\mathrm{H}}^{\mathrm{ORC,LB}}, T_{\mathrm{max}}^{\mathrm{TES}} - \Delta T_{\mathrm{HEX,TES}}^{\mathrm{min}}\right)$ $-h'\left(p_{\mathrm{L}}^{\mathrm{ORC,LB}}\right)$
$\Delta h_{\mathrm{comp}}^{\mathrm{HP}}$	$0.25\,\Delta h_{\mathrm{TES}}^{\mathrm{HP,LB}}$	$\Delta h_{\mathrm{TES}}^{\mathrm{HP,UB}}$
$T_{\mathrm{cold}}^{\mathrm{TES}}$	$323\,\mathrm{K}$	$616\,\mathrm{K}$
$T_{\mathrm{hot}}^{\mathrm{TES}}$	$323\,\mathrm{K}$	$616\,\mathrm{K}$
t_{max}^{+}	$4\,\mathrm{h}$	$24\,\mathrm{h}$
r	0.5	2

single-objective nonlinear program (NLP):

$$\min_{\boldsymbol{x}\in\mathbb{R}^{n_x}} \quad -R_{\mathrm{ANN}}\left(\boldsymbol{x}\right) \tag{8}$$

$$\text{s.t.} \quad C_{\mathrm{Cap}}\left(\boldsymbol{x}\right) \leq C_{\mathrm{Cap},i} \tag{9}$$

$$\boldsymbol{h}_{\mathrm{Design}}\left(\boldsymbol{x}\right) = \boldsymbol{0} \tag{10}$$

$$\boldsymbol{g}_{\mathrm{Design}}\left(\boldsymbol{x}\right) \leq \boldsymbol{0}. \tag{11}$$

We formulate the optimization model in reduced space (RS). This was shown to often be computationally superior compared to the full-space formulation for optimizing process flowsheets such as Rankine cycles in Bongartz and Mitsos (2017). As in our previous work (Lüthje et al. 2026), we add the HP compressor enthalpy difference as an additional optimization variable to improve computational performance. Thus, our model has one fewer degrees of freedom (DoFs) than the number of optimization variables. We summarize the optimization variables and their bounds in Tab. 6. In the model formulation, the revenue prediction (eq. 8), the CAPEX (eq. 7,9), and all constraints (eq. 10,11) are written as explicit functions of these optimization variables.

We choose the bounds on the optimization variables to reduce the feasible space as much as possible while still covering all sensible CB designs. We set the upper bounds on the storage medium temperatures, $T_{\mathrm{cold}}^{\mathrm{TES}}$ and $T_{\mathrm{hot}}^{\mathrm{TES}}$, to the maximum allowed temperature of Therminol 66 as given in Zhao et al. (2022) (616 K). The lower bound is the minimum temperature at which the storage medium remains in the transient or turbulent flow regime within the heat exchangers with the assumed geometry and flow velocity.

The DGO of the CB model is computationally challenging due to the large search space and highly nonlinear objective function and constraints. To improve computational performance, we implement reliability branching (Achterberg et al. 2005) into MAiNGO and use it for our case study. In reliability branching, the solver decides between strong branching and branching according to pseudocosts based on a reliability score η that represents the number of pseudocost updates for a specific variable. When the reliability score is below a user-specified threshold η_{rel}, strong branching is performed. If the threshold is exceeded, the pseudocosts are considered reliable, and the branching direction is selected based on pseudocosts alone. Previously, MAiNGO selected the branching variable based on the smallest relative diameter at the current node.

3.4 Implementation

We implement the data generation, ANN training, and optimization model in Python. As thermodynamic library, we use REFPROP 10.0 (Lemmon et al. 2018). Compared with the open-source alternative CoolProp (Bell et al. 2014), which we used in our previous work, REFPROP supports the calculation of thermal conductivity and viscosity for the WFs considered in this work. Both properties are required for computing heat transfer coefficients. For the other properties, the difference between data computed via CoolProp or REFPROP is orders of magnitude smaller than the accuracy of the surrogate models. To solve the optimal operation problem, we use Gurobi 13 (Gurobi Optimization 2024). We use Tensorflow (Abadi et al. 2016) to train all ANNs, together with the Levenberg–Marquardt (LM) implementation of Di Marco (2020). We use the parallel version of MAiNGO v0.10.2 (Bongartz et al. 2018) for the DGO of the CB design problem. Reliability branching will be included in a future public release of MAiNGO. The ANNs are embedded into the optimization problem using MeLOn v0.1.0 (Schweidtmann et al. 2019). As branching variable selection strategy, we apply reliability branching with a reliability threshold $\eta_{\mathrm{rel}} = 32$. All MAiNGO optimizations are performed on 48 cores of a CLAIX 2023 node of the RWTH high performance cluster (HPC). We set a wall-clock time limit of 10 min and a relative optimality gap of 1 %. During pre-processing, we perform 50 local searches.

3.5 Case study

In our previous work (Lüthje et al. 2026), we screened 20 different WFs for the use in HP and ORC of the CB. Since HP and ORC can use different WFs, this resulted in 400 combinations of HP WF and ORC WF that were screened. However, many of the considered WFs exhibit unfavorable characteristics, including high toxicity, global warming potential (GWP), and ozone depletion potential (ODP). Filtering such WFs leaves us with 10 WFs (100 combinations). For

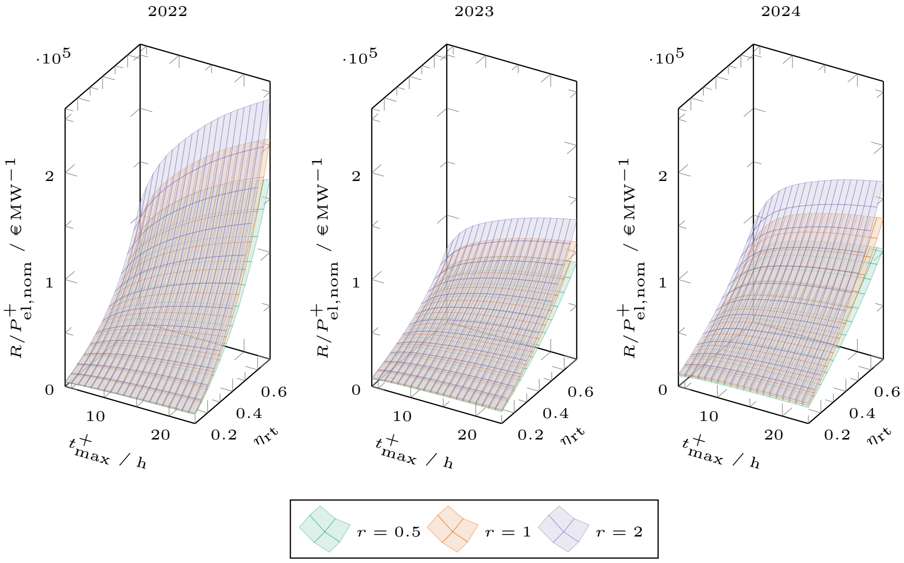

Figure 3: CB revenue per installed MW of charging power for the years 2022, 2023, and 2024

this work, we restrict our analysis to 2 WF combinations identified as promising in our previous work. First, ethylene oxide as both HP and ORC WF as a benchmark for CBs without restrictions on the WF selection. Representing the restricted WF selection as described above, we select cis-2-butene as both HP and ORC WF for the second case study. Using the same WF for both the charging and discharging process has the advantage that fewer ANNs for the property prediction have to be trained. To prevent excessive heat exchanger areas, we set the minimum temperature differences in all heat exchangers to 3 K. We assume the ambient temperature (i.e., the cooling water inlet temperature) to be $T_{\mathrm{amb}} = 15\,^{\circ}\mathrm{C}$. We fix the temperature change that the cooling water experiences in the ambient heat exchangers to 5 K. For the pay-off time and the interest rate, we assume $y = 25\,\mathrm{yr}$ and $f_{\mathrm{i}} = 3.49\,\%$ (Koksharov et al. 2024). We select a nominal charging power of 50 MW.

4 Results

4.1 Operation

Tab. 7 shows statistics of the price profiles we consider. Although the profiles are from subsequent years, they differ strongly. In 2022, the European gas crisis led to a much larger mean price and standard deviation than in the other years. The price profile of 2023 exhibits the lowest standard deviation (both absolute and relative to the mean). 2024 has the lowest prices but the highest coefficient

Table 7: Statistics of German day-ahead price profiles

Year	2022	2023	2024
Mean (€ $\mathrm{MW}^{-1}\,\mathrm{h}^{-1}$)	235.45	95.18	78.51
Standard deviation (€ $\mathrm{MW}^{-1}\,\mathrm{h}^{-1}$)	142.81	47.58	52.73
Coefficient of variation (%)	60.65	50.00	67.16
Number of hours with negative prices	69	301	457

of variation (ratio of standard deviation to mean). Also, this profile has the highest number of prices with negative hours ($\approx 5\,\%$ of all hours).

In Fig. 3, we present the optimal CB revenue (i.e., the solution of the optimal operation problem eqs. 1-6) as a function of the three battery parameters and the year. Note that we show the optimization results, not the ANN predictions. To aid in visualization, we discretize r into three values. Increasing the charge/discharge ratio r relaxes the discharge constraints (eq. 3). Thus, revenue always increases. Similarly, increasing the maximum charging time $t^{+}_{\max}$ (i.e., the storage size) relaxes the storage constraint (eq. 4) and increases revenue. Increasing efficiency allows for the discharge of more electricity for a fixed operating profile. Thus, revenue increases as long as the electricity is discharged during times with nonnegative electricity prices. Our results match this analysis. The revenue increases monotonically with $t^{+}_{\max}$, r, and the RTE. The year 2022 exhibits the largest revenues. For a CB with all battery parameters at their upper bound, the maximum revenue of 2022 is 86 % larger compared to 2023 and 46 % larger compared to 2024. This can be partly explained by the large standard deviation of the electricity price. Of the considered years, 2022 benefits most from a high RTE. For a CB with $t^{+}_{\max} = t^{-}_{\max} = 12\,\mathrm{h}$, increasing the RTE from 50 % to 60 % increases revenue in 2022 by 46 % compared to 30 % and 27 % in 2023 and 2024, respectively. Also, the benefit of increasing the maximum charge time $t^{+}_{\max}$ (i.e., the storage capacity) is largest for 2022. For a CB with $t^{+}_{\max}$ and the RTE at their upper bound, increasing r from 0.5 to 2 increases the revenue by 45 % in 2022, 44 % in 2023, and 61 % in 2024. The larger benefit of oversizing the discharging process in 2024 likely stems from the higher number of hours with negative prices in 2024. Increasing the maximum discharge power allows shifting a large fraction of the discharging hours into hours with negative prices. This might also explain why 2024 shows the largest revenue for CBs with small RTEs.

In the SI, we also show the optimal revenues obtainable when additionally providing FCR. We observe the largest absolute revenue increases in 2022 and 2024 for highly efficient CBs with small storage sizes. The relative revenue increase is largest (up to 30 %) for highly inefficient CBs. However, for reasonably efficient CBs ($\eta_{\mathrm{rt}} \geq 50\,\%$) with at least moderate storage ($t^{+}_{\max} \geq 8\,\mathrm{h}$) the revenue increase is small, not exceeding 5 %. This is likely due to the low maximum reserved capacity and the restriction on mode switches during FCR provisioning.

Table 8: Average prices used for the LCOE objective function

Year	$\overline{c}_{\mathrm{el,LCOE}}\left[€\,\mathrm{MW}^{-1}\,\mathrm{h}^{-1}\right]$
2022	160.96
2023	57.18
2024	38.01

4.2 Design

In this section, we analyze the influence of accounting for operational revenue in the design optimization. We optimize the CB design along the Pareto front between CAPEX minimization and revenue maximization. Further, we compare against two objective functions used in literature to optimize the CB design:

- Tillmanns et al. (2022) minimize the SIC, defined as the ratio of total investment costs to the energy discharged over a full discharging period:

  $$\mathrm{SIC} = \frac{C_{\mathrm{GR}}}{P^{-}_{\mathrm{el,nom}} t^{-}_{\max}}$$

  The authors implement constraints on the charging and discharging time, limiting the charging time to 8 h and the cycle length to 24 h:

  $$\begin{aligned} t^{+}_{\max} &\leq 8\,\mathrm{h} \\ t^{+}_{\max} + t^{-}_{\max} &\leq 24\,\mathrm{h} \end{aligned}$$

  This objective function does not consider any market information.

- Koksharov et al. (2024) assume maximum charging and discharging time to both be 4 h ($t^{+}_{\max} = t^{-}_{\max} = 4\,\mathrm{h}$) and a single daily charging/discharging cycle, based on the characteristic operating profile determined by Dietrich (2017). They then optimize the LCOE:

  $$\mathrm{LCOE} = \frac{C_{\mathrm{GR}} + \sum_{t=1}^{n} \frac{A_t}{(1+i)^t}}{\sum_{t=1}^{n} \frac{365\, t^{-}_{\max}\, P^{-}_{\mathrm{el,nom}}}{(1+i)^t}} + \frac{\overline{c}_{\mathrm{el,LCOE}}}{\eta_{\mathrm{rt}}}$$

  The LCOE represents the average cost of the discharged electricity. We compute the annual operation and maintenance costs as $A_t = 0.015\, C_{\mathrm{GR}}$ (Koksharov et al. 2023). This objective function incorporates market information in the form of the average electricity price $\overline{c}_{\mathrm{el,LCOE}}$ for the cheapest consecutive 4 h block of each day in the considered year. We determine this price for the considered years according to the procedure presented in Dietrich (2017) (cf. Tab. 8) prior to the optimization.

Besides the SIC and the LCOE, further objective functions are used in literature. Examples for these are the RTE (which we used in our previous work)

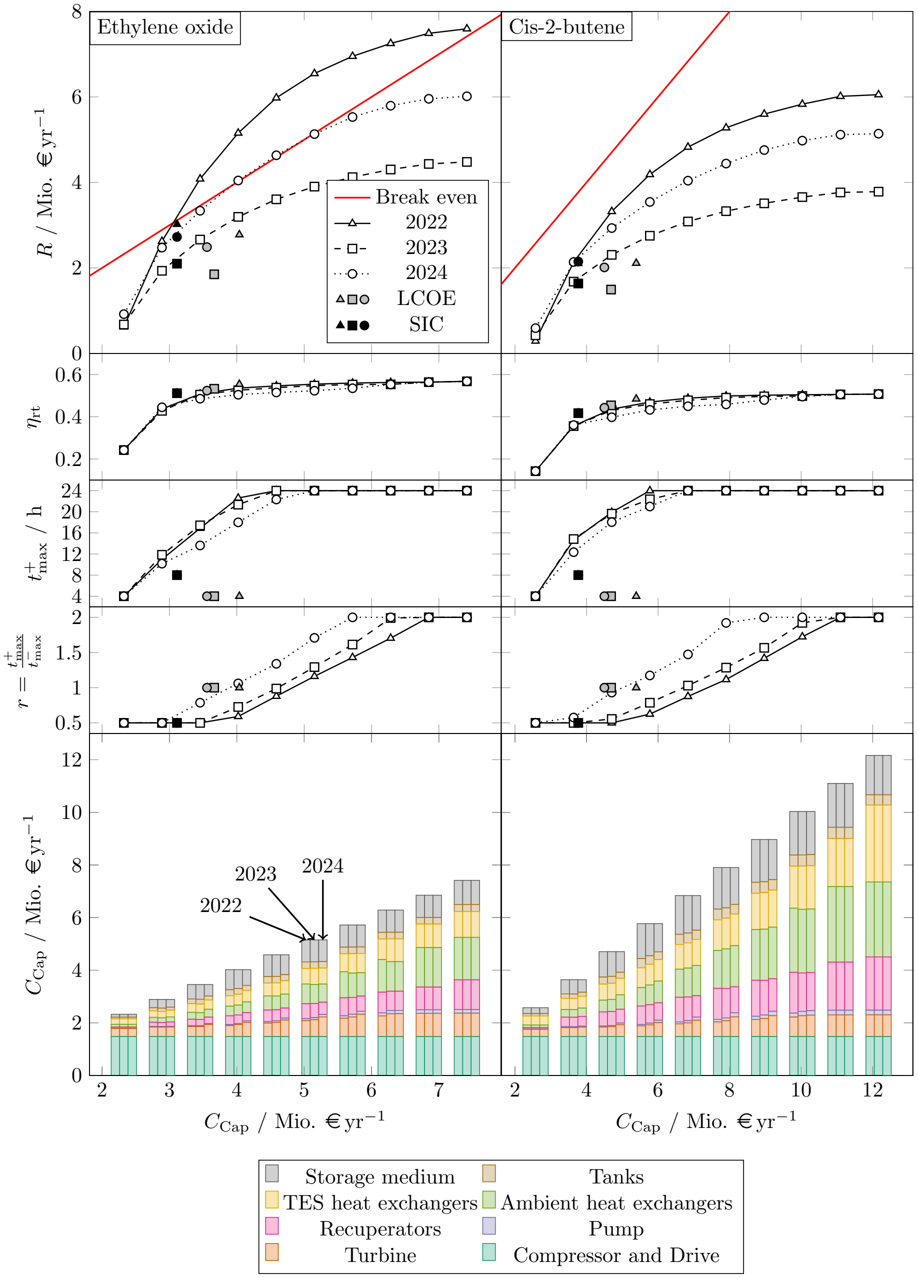

Figure 4: Pareto fronts for a CB using either ethylene oxide or cis-2-butene as WF without FCR provision. Note that, although both x-axes show the CAPEX, different axis scalings are used for the two WFs.

and the specific work $\omega_M = P_{\mathrm{el}}^{-}/\dot{m}_{\mathrm{WF}}^{-}$ (Rech et al. 2025). However, these objectives are independent of the absolute and relative sizing of HP, ORC, and TES. Thus, we do not include them in the comparison.

We show the Pareto fronts for ethylene oxide as WF and for cis-2-butene as WF in Fig. 4. A CB using ethylene oxide can achieve a profit over a wide range of maximum investment costs when considering the year 2022. For 2023, no profitable CB design exists. For 2024, operational revenue barely allows breaking even at a small region around 4.5 Mio. €$\,\mathrm{yr}^{-1}$ CAPEX. We briefly discuss the transferability of these results to other countries or future time periods in Sec. 5. When comparing the three considered years, we observe variations in the optimal battery parameters. While the battery parameters are identical at the extreme points (as explained above), they differ for intermediate points of the Pareto front. Comparing 2022 and 2024, in 2022 investing in increasing the RTE and storage size appears important, whereas in 2024 oversizing the discharging process is more cost-efficient. 2023 shows characteristics similar to 2022, with a slightly stronger emphasis on increasing r. Overall, the optimal results strongly favor investing in storage size, and the maximum value is reached quickly. Further, we observe that the RTE is the last battery parameter to reach its maximum value. This is likely due to the low temperature difference required for a very high RTE, resulting in high heat exchanger costs.

We also compare to the optimal solution obtained by minimizing either the LCOE or the SIC. The LCOE-optimal CB designs achieve substantially less revenue compared to scheduling-aware optimal CB designs with similar CAPEX. This effect is most pronounced when using 2022 data. In the battery parameters, we observe a large deviation from the Pareto-optimal designs due to the fixed storage size in the LCOE-optimization ($t_{\mathrm{max}}^{+} = t_{\mathrm{max}}^{-} = 4\,\mathrm{h}$). Also, for 2022, the LCOE-optimal solution contains a RTE near the thermodynamic maximum, which is incentivized by the average electricity price during charging $\overline{c}_{\mathrm{el,LCOE}}$. This price was more than twice as high in 2022 as in the other years (cf. Tab. 8). The actual revenue achievable for this price profile does not offset the CAPEX required for such a high RTE. The SIC do not depend on the considered price profile. Thus, the design (and battery parameters) are independent of the year; only the achievable earnings vary with the year. Surprisingly, optimizing the SIC yields CB designs that are much closer to the Pareto front than optimizing the LCOE. This can be partly explained by the larger storage size and the small relative size of the ORC, which is optimal for CBs with low-to-medium CAPEX. However, the SIC leads to CB designs with CAPEX too low to achieve profitability. Both objective functions overestimate the importance of a high RTE.

For a CB using cis-2-butene as WF, we observe similar trends. However, the investment costs are higher, so that the CB cannot achieve profitability for the considered price scenarios. Also, the maximum achievable RTE is lower (53.0 % compared to 58.6 %).

In the SI, we show the Pareto fronts when FCR provision is additionally allowed. The effect of providing FCR is small, as expected given that we assume that only 10 % of the nominal power can be provided as FCR. However, for cis-

2-butene, in 2022, the Pareto-optimal CB designs tailored to provide FCR reach the maximum storage size more quickly. For 2024, the maximum ORC size is reached earlier.

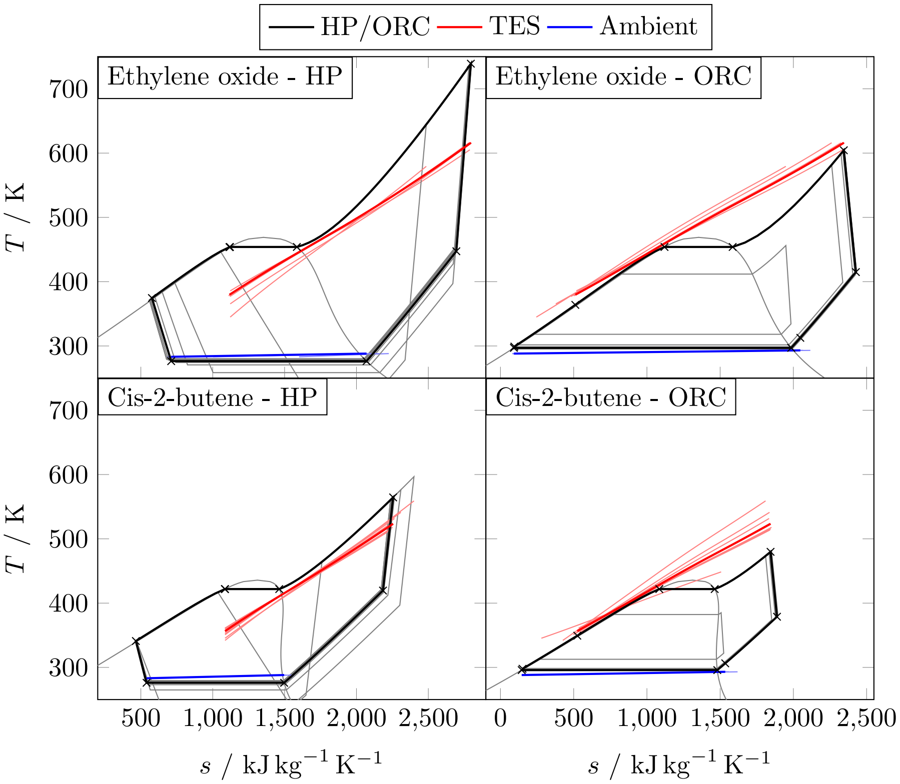

Figure 5: T-s diagrams of the CB. We show every Pareto point for the year 2022 (cf. Fig. 4). The Pareto point with the fifth lowest CAPEX is printed in bold.

Next, we analyze the T-s diagram of the Pareto-optimal CB designs for the electricity price profiles of 2022 (cf. Fig. 5). In the Pareto-optimal solutions, no subcooling occurs within the heat exchanger between HP and TES. This maximizes heat flow within the HP recuperator, thereby achieving the largest superheating of the compressor outlet. In the HP, the high pressure level is always at its upper bound. In the ORC, only the CAPEX-minimal solution has the high pressure level not at its upper bound. This indicates that increasing the upper bound of the high pressure level could improve economics. Also, transcritical operation might be promising. As CAPEX increases, the temperature difference across the ambient heat exchanger decreases, thereby increasing RTE.

We also see two reasons for the increased CAPEX when using cis-2-butene as WF. To minimize the cost of the storage medium (and tanks), the optimizer maximizes the temperature difference between the hot and cold TES tanks. A CB with ethylene oxide as WF achieves this well, as it can heat the storage medium to its maximum allowable bulk temperature (616 K). Thus, ethylene oxide can achieve higher temperature differences in the TES, thereby reducing storage costs. Cis-2-butene has a lower critical temperature and therefore does not reach the maximum storage medium temperature. Furthermore, in the Pareto-optimal solutions for cis-2-butene, the LMTD of the ORC preheater is low due to small temperature differences at both the in- and outlet, resulting in a high cost for the TES heat exchanger.

4.3 Computational performance

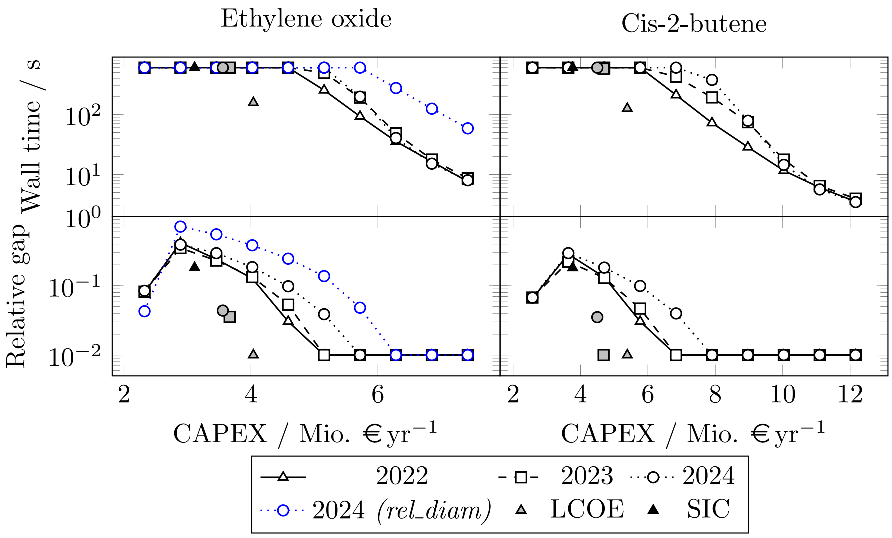

Figure 6: Wall-clock time and remaining relative gap for the CB design optimization runs. We also show the performance of the branching variable selection strategy according to the relative node diameter *(rel_diam)* for a CB using ethylene oxide in the year 2024. The results for minimizing the SIC are shown only for one year (2022), since the objective function, and thus the optimal point, are independent of the chosen year.

To analyze computational performance, we plot the wall-clock time and the remaining relative optimality gap in Fig. 6. The observed performance varies and worsens as CAPEX restrictions increase. When the CAPEX is limited to half the maximum CAPEX or less, most optimization runs fail to converge. The highest remaining gap after reaching the maximum wall-clock time is observed for a CB with ethylene oxide as WF for the Pareto point with the second-lowest CAPEX. Here, the remaining gap is 39 %. The CAPEX-minimal Pareto point (i.e., only minimizing CAPEX) reaches a lower gap. A possible explanation is that, for this optimization run, the two variables influencing sizing ($t^{+}_{\max}$ and r) are at their lower bounds in the optimal solution. For both WFs, the 2024 price profile exhibits the worst computational performance. Comparing the WFs, we observe better performance for cis-2-butene. Here, one more Pareto point can be solved to global optimality, and the remaining gaps for the other points are smaller. Although the LCOE is only affected by the price profile via a coefficient in the objective function ($\overline{c}_{\mathrm{el,LCOE}}$), the performance varies strongly with the considered year. Again, 2024 shows the slowest convergence. Optimizing the SIC leads to a remaining gap comparable to the worst Pareto point.

Finally, we compare reliability branching to selecting the branching variable based on the relative node diameter. We see a significant performance improvement, with wall-clock time reducing by a factor of ~ 7 for the instances that converge. As a result, one additional Pareto point converges when using reliability branching. In addition to this, reliability branching yields at least a 50 % smaller remaining gap for the instances that do not converge.

While some local multistart searches converge to local minima, branch-and-bound (B&B) never improves upon the best multistart solution.

5 Conclusion and outlook

We optimized the design and operation of Rankine-based CB using thermal oil as hot storage and the environment as cold storage. To reduce computational complexity, we solved the optimal operation problem offline for different CB parameters and trained a surrogate model predicting the optimal revenue as a function of the CB parameters. Then, we solved the operation-aware design optimization problem with the surrogate model embedded. Compared with the common literature approach of assuming a fixed daily operating profile, this method results in CB designs that achieve higher revenue at the same CB cost. Further, we replaced multiple model parts (thermodynamics, operation, and heat transfer) with surrogate models and embedded them into the model formulation. We computed the Pareto front between cost minimization and revenue maximization for a CB with a nominal charging power of 50 MW. Results show that a CB using ethylene oxide as WF and Therminol 66 as the storage medium could have been economically viable through price arbitrage in the German day-ahead market in 2022 and 2024. In contrast, using cis-2-butene as WF results in economically unfavorable designs due to lower RTE, higher heat exchanger costs, and a lower temperature difference between the storage tanks. These results are strongly dependent on the electricity price profile and thus transferring them to other countries or to future time periods is difficult. Mercier et al. (2023) investigated the day-ahead arbitrage potential for storage in all European bidding zones from 2000 to 2021, observing a drop in arbitrage potential over time, followed by an upward spike due to the European gas crisis. Further, the arbitrage potential is highly dependent on the present electricity generation technologies and thus location-specific. For Germany, prior to the gas crisis, Nitsch et al. (2021) predicted an increase in storage arbitrage revenue in a 2030 forecast scenario compared to 2019. In a recent study Geis et al. (2026) predicted the price development of German electricity prices from 2020 to 2045. In their scenario, volatility peaks in 2035, and there is a transition from distinct price levels set by fossil-based generation to a smooth price curve due to storage. Overall, it seems likely that economics for a CB in Germany will not worsen compared with the years considered. Solving the model to convergence was challenging and was not achieved for around half of the optimization runs for a wall time limit of 10 min using 48 cores. We demonstrated that reliability branching significantly improves computational performance for the DGO of RS models using MAiNGO.

As shown by our results, the low maximum RTE and the high cost associated with reaching this maximum RTE of Rankine-based CBs limit spot market revenue. The efficiency could be improved in multiple ways. Extension of the model to supercritical operation seems promising, as the upper pressure levels (p^H_{HP} and p^L_{ORC}) are almost always at their upper bounds, and most heat transfer to and from the TES occurs outside the two-phase region. Supercritical operation would enable the temperature profiles of the HP and ORC WF to more closely match the storage medium, resulting in higher efficiencies. This would require discretization of the TES heat exchangers (see, e.g., Huster et al. 2018). Another option to better match the temperature profile of WF and storage medium is to combine multiple (hot) storage systems (Dumont et al. 2020; Palacios et al. 2020). Extending our model by an additional TES would only require minor changes. However, more decision variables would be required, which would worsen computational performance. Next, including additional energy sources (e.g., waste heat) and energy outputs (e.g., heat from the TES for district heating) can improve the revenue and efficiency (Lykas et al. 2026). However, this limits feasible locations for the CB and imposes constraints on the operation.

Furthermore, off-design operation was identified as one of the key challenges for CBs (Dumont et al. 2020). For the considered CB, off-design operation would occur due to fluctuations in ambient temperature or when capacity for FCR is reserved. Such considerations can be incorporated into the design optimization via a two-stage stochastic program that accounts for multiple operating scenarios for a single design (e.g., Langiu et al. 2022). To extend our method to off-design operation, we would need to introduce additional parameters that describe the off-design behavior and incorporate them into the optimal operation problem.

References

50Hertz, Amprion, TenneT, and TransnetBW (2026). *Regelleistung.net.*

Abadi, M., Agarwal, A., Barham, P., Brevdo, E., Chen, Z., Citro, C., Corrado, G. S., Davis, A., Dean, J., Devin, M., Ghemawat, S., Goodfellow, I., Harp, A., Irving, G., Isard, M., Jia, Y., Jozefowicz, R., Kaiser, L., Kudlur, M., Levenberg, J., Mane, D., Monga, R., Moore, S., Murray, D., Olah, C., Schuster, M., Shlens, J., Steiner, B., Sutskever, I., Talwar, K., Tucker, P., Vanhoucke, V., Vasudevan, V., Viegas, F., Vinyals, O., Warden, P., Wattenberg, M., Wicke, M., Yu, Y., and Zheng, X. (2016). *TensorFlow: Large-Scale Machine Learning on Heterogeneous Distributed Systems.*

Achterberg, T., Koch, T., and Martin, A. (2005). "Branching rules revisited". In: *Oper. Res. Lett.* 33.1, pp. 42–54. ISSN: 0167-6377. DOI: `10.1016/j.orl.2004.04.002`.

Allman, A., Palys, M. J., and Daoutidis, P. (2019). "Scheduling–informed optimal design of systems with time–varying operation: A wind–powered ammonia case study". In: *AlChE J.* 65.7, e16434. ISSN: 1547-5905. DOI: `10.1002/aic.16434`.

Bahadori, A. and Vuthaluru, H. B. (2010). "Estimation of maximum shell-side vapour velocities through heat exchangers". In: *Chem. Eng. Res. Des.* 88.12, pp. 1589–1592. ISSN: 0263-8762. DOI: `10.1016/j.cherd.2010.04.001`.

Basán, N. P., Grossmann, I. E., Gopalakrishnan, A., Lotero, I., and Méndez, C. A. (2018). "Novel MILP Scheduling Model for Power-Intensive Processes under Time-Sensitive Electricity Prices". In: *Ind. Eng. Chem. Res.* 57.5, pp. 1581–1592. ISSN: 0888-5885. DOI: `10.1021/acs.iecr.7b04435`.

Bell, I. H., Wronski, J., Quoilin, S., and Lemort, V. (2014). "Pure and Pseudo-pure Fluid Thermophysical Property Evaluation and the Open-Source Thermophysical Property Library CoolProp". In: *Ind. Eng. Chem. Res.* 53.6, pp. 2498–2508. ISSN: 0888-5885. DOI: `10.1021/ie4033999`.

Benato, A. and Stoppato, A. (2018). "Pumped Thermal Electricity Storage: A technology overview". In: *Therm. Sci. Eng. Prog.* 6, pp. 301–315. ISSN: 2451-9049. DOI: `10.1016/j.tsep.2018.01.017`.

Bongartz, D., Najman, J., Sass, S., and Mitsos, A. (2018). *MAiNGO – McCormick-based Algorithm for mixed-integer Nonlinear Global Optimization.*

Bongartz, D. and Mitsos, A. (2017). "Deterministic global optimization of process flowsheets in a reduced space using McCormick relaxations". In: *J. Global Optim.* 69.4, pp. 761–796. ISSN: 1573-2916. DOI: `10.1007/s10898-017-0547-4`.

Bundesnetzagentur (2024). *Bundesnetzagentur — SMARD.de - Market data.* `https://www.smard.de/home/downloadcenter/download-marktdaten/`. Accessed: 30 September 2025.

Cebulla, F., Haas, J., Eichman, J., Nowak, W., and Mancarella, P. (2018). "How much electrical energy storage do we need? A synthesis for the U.S., Europe, and Germany". In: *J. Clean. Prod.* 181, pp. 449–459. ISSN: 0959-6526. DOI: `10.1016/j.jclepro.2018.01.144`.

Di Marco, F. (2020). *Tensorflow implementation of Levenberg-Marquardt training algorithm.*

Dias, L. S. and Ierapetritou, M. G. (2020). "Integration of planning, scheduling and control problems using data-driven feasibility analysis and surrogate models". In: *Comput. Chem. Eng.* 134, p. 106714. ISSN: 0098-1354. DOI: `10.1016/j.compchemeng.2019.106714`.

Dietrich, A. (2017). “Assessment of Pumped Heat Electricity Storage Systems through Exergoeconomic Analyses”. PhD thesis. TU Darmstadt. DOI: `10.26083/TUPRINTS-00006752`.

Dumont, O., Frate, G. F., Pillai, A., Lecompte, S., paepe, M. de, and Lemort, V. (2020). “Carnot battery technology: A state-of-the-art review”. In: *J. Energy Storage* 32, p. 101756. ISSN: 2352-152X. DOI: `10.1016/j.est.2020.101756`.

Geis, J., Neumann, F., Lindner, M., Härtel, P., and Brown, T. (2026). “Price formation in a highly-renewable, sector-coupled energy system”. In: *Energ. Econ.* 157, p. 109213. ISSN: 0140-9883. DOI: `10.1016/j.eneco.2026.109213`.

Gurobi Optimization, L. L. (2024). *Gurobi Optimizer Reference Manual*.

Huster, W. R., Schweidtmann, A. M., Lüthje, J. T., and Mitsos, A. (2020a). “Deterministic global superstructure-based optimization of an organic Rankine cycle”. In: *Comput. Chem. Eng.* 141, p. 106996. ISSN: 0098-1354. DOI: `10.1016/j.compchemeng.2020.106996`.

Huster, W. R., Schweidtmann, A. M., and Mitsos, A. (2018). “Hybrid Mechanistic Data-Driven Modeling for the Deterministic Global Optimization of a Transcritical Organic Rankine Cycle”. In: *Computer Aided Chemical Engineering : 13 International Symposium on Process Systems Engineering (PSE 2018)*. Ed. by M. R. Eden, M. G. Ierapetritou, and G. P. Towler. Vol. 48. Elsevier, pp. 1765–1770. DOI: `10.1016/B978-0-12-823377-1.50295-0`.

Huster, W. R., Schweidtmann, A. M., and Mitsos, A. (2020b). “Working fluid selection for organic rankine cycles via deterministic global optimization of design and operation”. In: *Optim. Eng.* 21.2, pp. 517–536. ISSN: 1573-2924. DOI: `10.1007/s11081-019-09454-1`.

Ikonen, T. J., Kim, B., Maravelias, C. T., and Harjunkoski, I. (2025). “Supervised Learning of the Optimal Objective Function Value in Chemical Production Scheduling”. In: *Ind. Eng. Chem. Res.* 64.8, pp. 4425–4438. ISSN: 0888-5885. DOI: `10.1021/acs.iecr.4c03045`.

Jacob, R., Hoffmann, M., Weinand, J. M., Linßen, J., Stolten, D., and Müller, M. (2023). “The future role of thermal energy storage in 100% renewable electricity systems”. In: *Renew. Sustain. Energy Transit.* 4, p. 100059. ISSN: 2667-095X. DOI: `10.1016/j.rset.2023.100059`.

Kahrs, O. and Marquardt, W. (2007). “The validity domain of hybrid models and its application in process optimization”. In: *Chem. Eng. Process.: Process Intensif.* 46.11, pp. 1054–1066. ISSN: 0255-2701. DOI: `10.1016/j.cep.2007.02.031`.

Koksharov, J., Klingelhofer, J., Dammel, F., and Stephan, P. (2023). “Thermodynamic and Economic Analysis of a Carnot Battery with a Two Zone Water Tank as Thermal Energy Storage”. In: *36th International Conference on Efficiency, Cost, Optimization, Simulation and Environmental Impact of Energy Systems (ECOS 2023)*. Ed. by J. R. Smith. Red Hook, NY: Curran Associates Inc, pp. 2126–2137. ISBN: 978-1-7138-7492-8. DOI: `10.52202/069564-0192`.

Koksharov, J., Zendel, L., Dammel, F., and Stephan, P. (2024). “Thermodynamic, Economic and Maturity Analysis of a Carnot Battery with a Two-

Zone Water Thermal Energy Storage for Different Working Fluids". In: *Energies* 17.2, p. 437. DOI: `10.3390/en17020437`.

Langiu, M., Dahmen, M., and Mitsos, A. (2022). "Simultaneous optimization of design and operation of an air-cooled geothermal ORC under consideration of multiple operating points". In: *Comput. Chem. Eng.* 161, p. 107745. ISSN: 0098-1354. DOI: `10.1016/j.compchemeng.2022.107745`.

Lemmon, E. W., Bell, I. H., Huber, M. L., and McLinden, M. O. (2018). *NIST Standard Reference Database 23: Reference Fluid Thermodynamic and Transport Properties-REFPROP, Version 10.0, National Institute of Standards and Technology.* DOI: `10.18434/T4/1502528`.

Liang, T., Vecchi, A., Knobloch, K., Sciacovelli, A., Engelbrecht, K., Li, Y., and Ding, Y. (2022). "Key components for Carnot Battery: Technology review, technical barriers and selection criteria". In: *Renew. Sustain. Energy Rev.* 163, p. 112478. ISSN: 1364-0321. DOI: `10.1016/j.rser.2022.112478`.

Locatelli, M. and Schoen, F. (2013). *Global optimization: Theory, algorithms, and applications.* Vol. 15. MOS-SIAM series on optimization. Philadelphia, Pa.: Mathematical Optimization Society and SIAM. ISBN: 978-1-61197-266-5. DOI: `10.1137/1.9781611972672`.

Ludwig, E. E. (2001). *Applied process design for chemical and petrochemical plants: A 3-volume set that emphasizes how to apply techniques of process control and interpret results into mechanical equipment details.* 3. ed. Vol. 3. Houston, Tex.: Gulf Publ. ISBN: 0884156516.

Lüthje, J. T., Langiu, M., and Mitsos, A. (2026). "Working fluid screening for ORC-based Carnot batteries by deterministic global optimization of design and nominal operation". In: *Optim. Eng.* 27.1, pp. 587–616. ISSN: 1573-2924. DOI: `10.1007/s11081-025-10026-9`.

Lykas, P., Bellos, E., and Tzivanidis, C. (2026). "Comprehensive review and performance assessment of Carnot battery storage systems with multiple energy outputs". In: *Energ. Convers. Manage.* 348, p. 120702. ISSN: 0196-8904. DOI: `10.1016/j.enconman.2025.120702`.

McCormick, G. P. (1976). "Computability of global solutions to factorable non-convex programs: Part I — Convex underestimating problems". In: *Math. Program.* 10.1, pp. 147–175. ISSN: 1436-4646. DOI: `10.1007/BF01580665`.

Mercier, T., Olivier, M., and Jaeger, E. de (2023). "The value of electricity storage arbitrage on day-ahead markets across Europe". In: *Energ. Econ.* 123, p. 106721. ISSN: 0140-9883. DOI: `10.1016/j.eneco.2023.106721`.

Modi, A. and Pérez-Segarra, C. D. (2014). "Thermocline thermal storage systems for concentrated solar power plants: One-dimensional numerical model and comparative analysis". In: *Sol. Energy* 100, pp. 84–93. ISSN: 0038-092X. DOI: `10.1016/j.solener.2013.11.033`.

Murty, K. G. (1980). "Computational complexity of parametric linear programming". In: *Math. Program.* 19.1, pp. 213–219. ISSN: 1436-4646. DOI: `10.1007/BF01581642`.

Najman, J., Bongartz, D., and Mitsos, A. (2019). "Relaxations of thermodynamic property and costing models in process engineering". In: *Comput.*

Chem. Eng. 130, p. 106571. ISSN: 0098-1354. DOI: `10.1016/j.compchemeng.2019.106571`.

Nitsch, F., Deissenroth-Uhrig, M., Schimeczek, C., and Bertsch, V. (2021). “Economic evaluation of battery storage systems bidding on day-ahead and automatic frequency restoration reserves markets”. In: *Appl. Energ.* 298, p. 117267. ISSN: 0306-2619. DOI: `10.1016/j.apenergy.2021.117267`.

Nitsch, F., Wetzel, M., Gils, H. C., and Nienhaus, K. (2024). “The future role of Carnot batteries in Central Europe: Combining energy system and market perspective”. In: *J. Energy Storage* 85, p. 110959. ISSN: 2352-152X. DOI: `10.1016/j.est.2024.110959`.

Palacios, A., Elena Navarro, M., Barreneche, C., and Ding, Y. (2020). “Hybrid 3 in 1 thermal energy storage system – Outlook for a novel storage strategy”. In: *Appl. Energ.* 274, p. 115024. ISSN: 0306-2619. DOI: `10.1016/j.apenergy.2020.115024`.

Poletto, C., Pascale, A. de, Ottaviano, S., Dumont, O., and Branchini, L. (2025). “Techno-economic assessment of a Carnot battery thermally integrated with a data center”. In: *Appl. Therm. Eng.* 260, p. 124952. ISSN: 1359-4311. DOI: `10.1016/j.applthermaleng.2024.124952`.

Psichogios, D. C. and Ungar, L. H. (1992). “A hybrid neural network–first principles approach to process modeling”. In: *AlChE J.* 38.10, pp. 1499–1511. ISSN: 1547-5905. DOI: `10.1002/aic.690381003`.

Rech, S., Danieli, P., Carraro, G., and Lazzaretto, A. (2025). “Multi-objective optimization of Pumped Thermal Energy Storage for large scale applications”. In: *Energy* 334, p. 137607. ISSN: 0360-5442. DOI: `10.1016/j.energy.2025.137607`.

Schäfer, P., Daun, T. M., and Mitsos, A. (2020). “Do investments in flexibility enhance sustainability? A simulative study considering the German electricity sector”. In: *AlChE J.* 66.11. ISSN: 0001-1541. DOI: `10.1002/aic.17010`.

Schäfer, P., Westerholt, H. G., Schweidtmann, A. M., Ilieva, S., and Mitsos, A. (2019). “Model-based bidding strategies on the primary balancing market for energy-intense processes”. In: *Comput. Chem. Eng.* 120, pp. 4–14. ISSN: 0098-1354. DOI: `10.1016/j.compchemeng.2018.09.026`.

Schmidt, O., Melchior, S., Hawkes, A., and Staffell, I. (2019). “Projecting the Future Levelized Cost of Electricity Storage Technologies”. In: *Joule* 3.1, pp. 81–100. ISSN: 25424351. DOI: `10.1016/j.joule.2018.12.008`.

Schweidtmann, A. M., Huster, W. R., Lüthje, J. T., and Mitsos, A. (2019). “Deterministic global process optimization: Accurate (single-species) properties via artificial neural networks”. In: *Comput. Chem. Eng.* 121, pp. 67–74. ISSN: 0098-1354. DOI: `10.1016/j.compchemeng.2018.10.007`.

Serth, R. W. (2007). *Process heat transfer: Principles and applications.* 1st ed. ScienceDirect. S.l., Amsterdam, and Heidelberg: ScienceDirect Online-Anbieter and Academic Press. ISBN: 9780123735881.

Steinmann, W. D. (2014). “The CHEST (Compressed Heat Energy STorage) concept for facility scale thermo mechanical energy storage”. In: *Energy* 69, pp. 543–552. ISSN: 0360-5442. DOI: `10.1016/j.energy.2014.03.049`.

Thulukkanam, K. (2013). *Heat Exchanger Design Handbook.* CRC Press. ISBN: 9780429105647. DOI: `10.1201/b14877`.

Tillmanns, D., Pell, D., Schilling, J., and Bardow, A. (2022). "The Thermo–Economic Potential of ORC–Based Pumped–Thermal Electricity Storage: Insights from the Integrated Design of Processes and Working Fluids". In: *Energy Technol.* 10.7, p. 2200182. ISSN: 2194-4288. DOI: `10.1002/ente.202200182`.

Torricelli, N., Branchini, L., Pascale, A. de, Dumont, O., and Lemort, V. (2023). "Optimal Management of Reversible Heat Pump/Organic Rankine Cycle Carnot Batteries". In: *J. Eng. Gas Turbines Power* 145.4. ISSN: 0742-4795. DOI: `10.1115/1.4055708`.

Towler, G. and Sinnott, R. (2013). *Chemical engineering design: Principles, practice, and economics of plant and process design.* Second edition. Amsterdam and Heidelberg: Elsevier Butterworth-Heinemann. ISBN: 1283396238.

Turton, R., Bhattacharyya, D., and Richard/Shaeiwitz, J. A. T. (2018). *Analysis, Synthesis, and Design of Chemical Processes.* 5th ed. [S.l.]: Pearson (IT Professional) and Pearson. ISBN: 0134177487.

Vecchi, A., Knobloch, K., Liang, T., Kildahl, H., Sciacovelli, A., Engelbrecht, K., Li, Y., and Ding, Y. (2022). "Carnot Battery development: A review on system performance, applications and commercial state-of-the-art". In: *J. Energy Storage* 55, p. 105782. ISSN: 2352-152X. DOI: `10.1016/j.est.2022.105782`.

Zhao, Y., Song, J., Liu, M., Zhao, Y., Olympios, A. V., Sapin, P., Yan, J., and Markides, C. N. (2022). "Thermo-economic assessments of pumped-thermal electricity storage systems employing sensible heat storage materials". In: *Renew. Energ.* 186, pp. 431–456. ISSN: 0960-1481. DOI: `10.1016/j.renene.2022.01.017`.